Microphysical characteristics and evolution of seeded orographic clouds

Katja Friedrich[1], Jeffrey R. French[2], Sarah A. Tessendorf[3], Melinda Hatt[2], Courtney Weeks[3], Robert M. Rauber[4], Bart Geerts[2], Lulin Xue[3], Roy M. Rasmussen[3], Derek R. Blestrud[5], Melvin L. Kunkel[5], Nicholas Dawson[5], and Shaun Parkinson[5]

[1] Department of Atmospheric and Oceanic Sciences, University of Colorado, Boulder, CO

[2] Department of Atmospheric Science, University of Wyoming, Laramie, WY

[3] Research Applications Laboratory, National Center for Atmospheric Research, Boulder, CO

[4] Department of Atmospheric Sciences, University of Illinois-Urbana/Champaign, Urbana, IL

[5] Idaho Power Company, Boise, ID

Submitted on 10 September to the Journal of the Applied Meteorology and Climatology

Corresponding Author: Katja Friedrich, University of Colorado Boulder, Department of Atmospheric and Oceanic Sciences, 4001 Discovery Drive, Boulder, CO, 80309. Email: Katja.Friedrich@colorado.edu

Abstract

The spatial distribution and magnitude of snowfall resulting from cloud seeding with silver iodide (AgI) is closely linked to atmospheric conditions, seeding operations, and dynamical, thermodynamical, and microphysical processes. Here, microphysical processes leading to ice and snow production are analyzed in orographic clouds for three cloud seeding events, each with light or no natural precipitation and well-defined, traceable seeding lines. Airborne and ground-based radar observations are linked to *in-situ* cloud and precipitation measurements to determine the spatiotemporal evolution of ice initiation, particle growth, and snow fallout in seeded clouds. These processes and surface snow amounts are explored as particle plumes evolve from varying amounts of AgI released, and within changing environmental conditions, including changes in liquid water content (*LWC*) along and downwind of the seeding track, wind speed, and shear. More AgI did not necessarily produce more liquid equivalent snowfall (*LESnow*). The greatest amount of *LESnow*, largest area covered by snowfall, and highest peak snowfall produced through seeding occurred on the day with the largest and most widespread occurrence of supercooled drizzle, highest wind shear, and greater *LWC* along and downwind of the seeding track. The day with the least supercooled drizzle and the lowest *LWC* downwind of the seeding track produced the smallest amount of *LESnow* through seeding. The stronger the wind, the farther away the snowfall occurred from the seeding track.

1. Introduction

Mountain snowpack is a natural reservoir recharged annually by winter snowfall. Seeding of orographic clouds to increase snowpack and water supplies for agricultural, energy and municipal applications has been pursued for nearly seventy years (Rauber et al. 2019). During cloud seeding, Silver iodide (AgI) aerosols are injected into clouds of supercooled liquid water (SLW) converting droplets into ice particles, which subsequently fall out as snow (Ludlam 1955). Advances in physical analyses of cloud seeding operations have recently resulted in increasingly robust evaluations of cloud seeding components under varying atmospheric conditions (e.g., Geerts et al. 2010; Geerts et al. 2013; Pokharel et al. 2014; Pokharel et al. 2017; French et al. 2018; Tessendorf et al. 2019; Friedrich et al. 2020). In orographic cloud systems, SLW forms within updrafts generated through orographic lift, convection, and dynamical processes such as gravity waves, cloud-top generating cells, or turbulence (see review by Rauber et al. 2019). Low ice particle concentrations (< 0.1 L^{-1}) and warm cloud tops ($> -15°C$) enhance the likelihood that SLW will be present (e.g., Politovich 1989; Rangno and Hobbs 1991; Murakami et al. 1992; Rasmussen et al. 1995; Cober et al. 1996; Geresdi et al. 2005). Targeting areas of enhanced SLW and low natural ice crystal concentrations by introducing artificial ice nucleating particles increase the likelihood that ice crystals may form and precipitate as snow.

Several studies have observed the airborne seeding-induced ice nucleation process by measuring an increase in in-cloud ice particle concentrations, changes in particle-size spectra, and depletion of smaller and growth of larger particles (Hobbs 1975; Hobbs et al. 1981; Deshler et al. 1990; Deshler and Reynolds 1990; French et al. 2018). However, quantifying ice and snow production, and comparing the results from seeding experiments remains challenging due to variations in the amount and type of seeding agent used, thermodynamic structure of the clouds, and atmospheric conditions during seeding. For example, Deshler and Reynolds (1990) observed an ice particle concentration of 50–100 L^{-1} and rimed particles 5-10 min after airborne cloud seeding over California's central Sierra Nevada using a combination of dry ice and AgI. By contrast, French et al. (2018) reported an ice particle concentration of only 1-5 L^{-1} with diameters > 300 μm 30 min after airborne seeding using AgI over Idaho's Payette mountains. Once ice nucleation occurs, ice particles undergo depositional, dendritic growth at temperatures between -10° and -15°C (Takahashi et al. 1991; Fukuta and Takahashi 1999; Kennedy and Rutledge 2011; Andrić et al. 2013; Bechini et al. 2013; Schrom et al. 2015; Williams et al. 2015; Moisseev et al. 2016; Griffin et al. 2018) as well as aggregation and riming (Reinking 1979; Mitchell et al. 1990; Harimaya and Sato 1989; Moisseev et al. 2017; Grazioli et al. 2015).

Although these studies have provided evidence of microphysical changes associated with cloud seeding, in this study ice initiation and snow production are quantified and linked to environmental conditions, seeding procedures, and microphysical processes. The goal of this paper is to quantify ice and snow production, and associated microphysical processes due to cloud seeding, and show how these processes are linked to environmental conditions, terrain, and AgI amount for three cloud seeding events discussed previously in French et al. (2018), Tessendorf et al. (2019), and Friedrich et al. (2020). We attempt to answer the following questions (Fig. 1): How much SLW is depleted and ice produced in seeded clouds? How long does it take to produce ice after AgI injection into clouds? How fast does ice grow into precipitating snow? How are ice initiation, particle growth, and snow fall out related to the amount of AgI released and environmental conditions?

2. SNOWIE campaign

Data for these events were collected on 19, 20, and 31 Jan 2017 during the Seeded and Natural Orographic Wintertime Clouds: The Idaho Experiment (SNOWIE). On those days, the seeding aircraft released burn-in-place (BIP) and/or ejectable (EJ) flares of AgI perpendicular to the mean wind direction and upwind of two X-Band ground-based radars located on mountaintops at Packer John (PJ) and Snowbank (SB, Fig. 2, Table 1). Flight legs of the seeding aircraft will be referred to using capital letters, e.g., Leg A. The University of Wyoming King Air (UWKA) research aircraft flew tracks prior to, during, and after cloud seeding along the direction of the mean wind perpendicular to the seeding aircraft legs, passing over PJ (Fig. 2). Flight legs of the UKWA will be referred to using numbers (e.g., Leg 1). The PJ and SB radars conducted vertical cross section and volume scans (Table 2). Airborne *in-situ* and cloud radar observations are used to quantify supercooled liquid and natural ice particle concentrations prior to injecting AgI into the clouds, and ice nucleation resulting from cloud seeding. Dual-polarization radar observations from the PJ and SB radars are used to study microphysical processes. A detailed overview of the experimental design, instrument specifications, and deployed strategies is given in Appendix A and Tessendorf et al. (2019).

3. Ice initiation and snow growth on 19 January

a. Natural cloud characteristics and atmospheric conditions

During this event, a slightly conditionally unstable atmosphere was observed between 4-4.5 km at temperatures (*T*) between -12 and -18 °C (Fig. 3a-b, blue lines, all heights above mean sea level, unless otherwise indicated). Southwesterly flow < 20 m s^{-1} was observed between the surface and 4 km veering to southerly flow between 5.5 km and 7 km where winds increased from 20 to 38 m s^{-1} (Fig. 3c). Enhanced wind shear of > 0.02 s^{-1} occurred between the surface-2 km and 4-4.5 km. Prior to seeding, cloud top was > 8 km MSL. This deeper cloud split into two layers, with seeding occurring in the lower cloud layer, which had a top between 4 to 4.5 km. During seeding, the cloud top of the lower layer descended to about 3 km as shallower clouds moved in from the west. Within the shallower cloud layer, tops varied as much as 1 km along a single flight leg. Clouds in which seeding lines were observed had $-13 < T < -15$ °C with cloud top at 4-5 km.

The UWKA flew repeated legs in-cloud within 1 km of cloud top at $-11 < T < -14$ °C. Natural cloud conditions were determined prior to seeding, and during and after seeding outside of the seeding lines. Clouds were dominated by SLW, with leg-averaged, *LWC*s ranging from 0.1 to 0.2 g m^{-3} and maxima ranging between 0.3 to 0.4 g m^{-3}. Cloud droplet concentrations were < 30 cm^{-3}. Supercooled drizzle with 50 μm < D < 100 μm, was observed in isolated pockets similar to natural conditions in other cases from SNOWIE (Tessendorf et al. 2019; Majewski and French 2020). Natural ice particle concentrations were < 1 L^{-1} and often < 0.1 L^{-1}. The only significant concentrations of ice observed at flight level were within seeding lines and over the highest terrain more than 40 km downstream of PJ.

b. Seeding operations and evolution of the seeding lines

The seeding aircraft flew six legs (Legs A-F) between 1620-1737 UTC (Fig. 2). The reflectivity plumes and microphysical signatures developing from those six legs will be referred to as Lines A' - F'. Legs A-B were flown at cloud top (4.1 km) with a mean temperature $\overline{T}$ = -14 °C (Fig. 4a). Legs C-F were flown at 4.4 km MSL at $\overline{T}$ = -16°C (Fig. 4a). Legs B-F were flown on a track downwind from A (Fig. 2). Leg A commenced at 1620 UTC. The *LWC* ranged from

0-0.4 g m^{-3} with $\overline{LWC}$ = 0.11-0.17 g m^{-3} along A and B, with lower amounts ($\overline{LWC}$ = 0.08-0.09 g m^{-3}) along C-D, mostly confined to the southeastern end of the track (Fig. 4a, Table 1). Negligible SLW ($\overline{LWC}$ < 0.008 g m^{-3}) was observed during E-F. Both BIP and EJ flares were deployed during all legs (Table 1, Fig. 4a).

A line of enhanced reflectivity (Z_e > 15 dBZ$_e$, surroundings = -30 to +10 dBZ$_e$) was first observed at 1647 UTC by the PJ DOW radar on the southern edge of the radar observational domain (ROD). Calculations of transport time of the seeding material by the mean wind showed that this line originated at A (and hence will be referred to as A') where EJs and BIPs were deployed 28 minutes earlier (Table 1). A' continued to move northeastward with the mean wind, passing over PJ at 1710 UTC (Fig. 5, Movie 1a). A second line of enhanced reflectivity (Z_e > 15 dBZ$_e$ surroundings = < -30 to +10 dBZ$_e$), associated with Leg B, was later observed on the southeastern side of the ROD at 1705 UTC, 15 minutes after the southern portion of B was flown (Fig. 5a). Recall that the seeding aircraft moved its flight track eastward after A (Fig. 2). As a result, A' and B' appeared as two parallel lines of enhanced reflectivity with A' upwind of B'. By the time A' and B' propagated through the ROD by 1812 UTC, and moved over higher terrain, the lines had widened and near surface Z_e within the lines enhanced to > 25 dBZ$_e$. Snowfall on the ground was first observed at 1715 UTC and continued through 1812 UTC (Fig. 3 in Friedrich et al. 2020).

The UWKA WCR first detected A' at 1650 UTC, ~12 km upwind of PJ on UKWA Leg 4. At this time, the ice particle plume associated with A' had a maximum Z_e of 5 dBZ$_e$ compared to Z_e < -10 dBZ$_e$ in surrounding regions. A' was 1-2 km wide and located at 4-5 km MSL (Fig. 6). Over the next 30 min, A' grew to 3-5 km wide in the upper portion of the cloud and Z_e increased to 10 dBZ$_e$. The plume of Z_e associated with A' extended from cloud top to the surface by 1719 UTC, 8 km downwind of PJ (Fig. 6, Leg 6). As precipitation descended to the ground, wind shear caused the near-surface portion of the Z_e plume to lag the upper-level portion so that A' appeared tilted (Fig. 6, Legs 7-8). During UWKA Legs 6-10, near-surface Z_e increased from 5 to 15 dBZ_e as A' passed over higher terrain. B' was observed by the WCR for the first time at 1717 UTC, 15 km downwind of PJ between 3.5 - 4.5 km MSL (Fig. 6, Leg 6). Similar to A', snow began to fall out during the next 30 minutes. Within B', Z_e reached a maximum 15 dBZ_e as it propagated over higher terrain. In both A' and B', Z_e at 3-4.5 km remained between 5-15 dBZ_e for up to 80 minutes after the seeding material was released, indicating continued particle nucleation and growth in the upper portion of the cloud. Both lines became tilted once the precipitation plume descended below ~3 km due to wind shear between the surface and higher altitudes.

Continuous lines of enhanced reflectivity were not identified from seeding legs C-F. These lines would have been expected to form upwind of A'. Cross-sections from the WCR for UWKA Legs 6-10 showed a significant decrease in cloud top, from 4.5 km during the time of Legs A-B to < 3 km when Legs C-F were flown. Seeding material from flares released during legs C-F at 4.4 km would not have reached the cloud top and, therefore, no lines developed.

c. Ice initiation and particle growth

During Legs 4-10, the UWKA made repeated passes through A' and B', 0.5 to 1 km below cloud top with $-11 < T < -14$ °C, near or below the level at which the AgI was released (Fig. 6). Seven (five) passes were made through A' (B'), ranging from 5 to 95 minutes after the seeding occurred. On Leg 4, 20 minutes after seeding occurred, the UWKA was 1 km below cloud top at $T = -11$ °C and the WCR detected A' above flight level with Z_e ~5 dBZ_e. Z_e at flight level was -15 dBZ_e, indicating the precipitation in A' had not yet descended to flight level (Fig. 7c, Leg 4). The cloud at flight level consisted of liquid cloud droplets 20 to 30 um in diameter (*D*), and was nearly devoid of ice particles (Fig. 7a,b; Leg 4). The *LWC* was between 0.01-0.05 g m^{-3} directly beneath the seeding line and as high as 0.08 g m^{-3} a few km downwind. During Leg 5, 10 minutes later at the same level, measurements within A' showed that the seeding line had descended through the flight level and reflectivity had increased to 10 dBZ_e (Fig. 7c, Leg 5). Consequently the concentration of cloud droplets ($D < 50$ um) had been depleted and the concentration of larger, ice particles ($D > 100$ um) had increased by two orders of magnitude (Fig. 7a,b; Legs 4-5). The observed *LWC*s within A' at this time were < 0.01 g m^{-3} and ice water contents (*IWC*) were > 0.10 g m^{-3}. A marked and rapid transition from liquid dominated to ice dominated cloud in A' had occurred at this level in just 10 minutes. Few pristine ice crystals were observed just after this transition during Leg 5 and most of the ice appeared to be irregularly shaped, suggesting some amount of riming had occurred (Fig. 7b, Leg 5). Another five passes through A' were made over the ensuing 60 minutes in Legs 6-10, and in all cases the observed *LWC* remained < 0.01 g m^{-3} (Fig. 7c, Legs 6-10) and the concentration of hydrometeors $D < 50$ μm remained < 1 cm^{-3}. However, the concentration of larger ice particles continued to exceed, by two orders of magnitude, the concentration observed during the earliest pass and in regions just upwind and downwind of A'. By 50 minutes after seeding, 2DS images confirmed the presence of dendritic crystals within A' (Fig. 7b, Leg 6). Dendritic crystals were observed in all subsequent legs within A', interspersed with irregular shaped ice (Fig. 7b, Legs 7-10).

Observations within B' suggest a similar microphysical evolution (Fig. 8). During UWKA Legs 4-5, at 5 and 15 minutes after seeding, no reflectivity signature was detected by the WCR (Fig. 8c, Legs 4-5). For these legs, we estimated the *expected* location of B' (had it been detected) using the AgI release time, location along B, and assumed that B is being advected with the mean wind at flight level. During Leg 4, the UWKA measured *LWC* in this region was 0.03 g m^{-3}. A significantly smaller amount of *LWC* was observed in Leg 5 and likely resulted from a local lowering of the cloud top. *LWC*s just a few km on either side of this were between 0.03-0.08 g m^{-3} (not shown). During both Legs 4-5, the clouds at flight level were nearly devoid of ice and dominated by relatively small supercooled liquid droplets (Fig. 8b, Legs 4-5). B' was detected by the WCR with a reflectivity of 5 dBZ_e during Leg 6, 30 minutes after seeding (Fig. 8c, Leg 6). *LWC* within B' at flight level was 0.01 g m^{-3}, particle images revealed some rimed ice, and particle size distributions showed a decrease in concentration of cloud droplets and an increase in larger hydrometeors (Fig. 8a-c, Leg 6). Of the four remaining Legs 7-10, only during Leg 9 was the *LWC* > 0.01 g m^{-3} within B' (Fig. 8c, Legs 7, 8, 10). During this leg, 75 minutes after seeding, cloud *LWC*s up to 0.03 g m^{-3} were observed, over higher terrain, nearly 60 km downwind of where the AgI was released. These higher *LWC*s were collocated in regions of ice hydrometeors concentrations of 2 - 3 L^{-1} (Fig. 8a, Leg 9) resulting in particle images that appear more irregular and hence more rimed than was observed throughout much of A'. For observations in both A' and B', total ice concentrations with D > 100 um, never exceeded 21 L^{-1}. Also, once ice was initiated within the A' and B', size distributions for ice hydrometeors with D > 1 mm (Figs. 7a and 8a) were remarkably consistent across all penetrations. Crystals of this size likely resulted from aggregation of smaller, dendritic ice crystals leading to the development of an exponential size distribution of these larger particles (Field and Heymsfield 2003)

d. Snow growth and fallout

As the seeding lines passed through the ROD, ice crystals and snow continued to grow, generating snowfall on the ground (Fig. 9). Between the first detection of A' by the PJ radar at 1654 UTC (15 min after seeding) and the time A' passed over PJ at 1706 UTC (36 min after seeding), Z_e and Z_{dr} increased from 3 to 7 dBZ_e and 0.6 to 1.8 dB, respectively (Fig. 9a). Between 25-40 min after seeding, the values of $Z_e < 10$ dBZ_e and $1 < Z_{dr} < 1.5$ dB near cloud top (3-4 km, $-8 < T < -12$°C) suggest that snow most likely grew through water vapor deposition (Ryzhkov and Zrnić 1998; Moisseev et al. 2009; Kennedy and Rutledge 2011; Bechini et al. 2013; Schneebeli et al. 2013). Within 40 minutes after seeding, weak up- and downdrafts (1-2 m s^{-1}) were observed within A' by the WCR (Fig. 10, UWKA Leg 6). A change in dual-polarization variables started 48 minutes after seeding (1718 UTC) and lasting for 15-20 minutes (Fig. 9). Near cloud top (3-4.5 km MSL), pockets of enhanced K_{dp} (> 1 ° km^{-1}) and Z_{dr} (0.6-1.2 dB) with updrafts up to 1.5 m s^{-1} were present. The updrafts near cloud top (Fig. 10, Leg 8) may be associated with additional orographic lift that A' experienced moving up the North Folk Range between 1724-1748 UTC after passing PJ (Fig. 9).

The dendritic growth layer (DGL) can be identified from dual-polarization observations as an enhancement in Z_{dr} and K_{dp}, reduced ρ_{hv}, and a strong vertical gradient in Z_e (e.g., Hogan et al. 2002; Kennedy and Rutledge 2011; Lamb and Verlinde 2011; Andrić et al. 2013; Bechini et al. 2013). These changes occur because dendrites enable rapid aggregational snow growth as the crystal branches more readily interlock (Pruppacher and Klett 1997). The enhancement in K_{dp} and Z_{dr} near cloud top occurred within $-10 < T < -15$°C where vigorous growth of dendritic ice particles is expected (Takahashi et al. 1991; Fukuta and Takahashi 1999). Enhanced dendritic growth near cloud top, starting at about 36-48 minutes after seeding, was also supported by images of particles from the 2DS which showed more dendritic crystals during Leg 6 (50 min after seeding) compared to Leg 5 (30 min after seeding; Fig. 7b). In fact, this enhancement of K_{dp} (> 1 ° km^{-1}) and Z_{dr} (0.6-1.2 dB) around 3.8 km or -13°C was observed along the length of A' as the line encountered higher terrain between 1724-1748 UTC 54-78 min after seeding (not shown). Z_{dr} and K_{dp} ranged mainly between -7 and 0 dB and 0 - 0.5 ° km^{-1}, respectively, between 1654-1712 UTC, while positive Z_{dr} and K_{dp} up to 1.5 dB and 1.6 ° km^{-1} was observed after 1718 UTC. Within the DGL, steady weak updrafts up to 1.5 m s^{-1} were observed (Fig. 10, Leg 7). These updrafts were likely associated with additional orographic lift that A' experienced as it passed the peak of the North Folk Range at 1730-1742 UTC (Figs. 9a and 10, Legs 7-8). As the clouds associated with A' passed through the ROD, reflectivities remained between 0-9 dBZ$_e$ at cloud top (3-4 km MSL). While no information of AgI concentration downwind of PJ is available, it is hypothesized that ice initiation continuously occurred as unactivated residual AgI was transported farther downward and updrafts, associated with higher terrain, provided *SLW* during local orographic ascent. As precipitation descended to the ground, wind shear caused the near-surface portion of A' to lag the upper-level portion so that A' appeared tilted (Fig. 9a). The snow associated with A' reached the ground within 42-48 min after seeding with Z_e > 10 dBZ$_e$, K_{dp} < 0.5° km^{-1}, and downward V_r of 3 m s^{-1} below 2 km MSL (Fig. 10). These values suggest heavily rimed particles.

Similar evolution and microphysical processes were observed within B' (Fig. 9b). B' was first observed at 1706 UTC (~20 min after cloud seeding) at 4-4.5 km MSL downwind of PJ, but still upwind of the North Fork Range (Fig. 2). As B' passed over the upwind side of the North Fork Range, Z_e and Z_{dr} increased from 1 to 10 dBZ$_e$ and 0.3 to 1.8 dB, respectively. Passage of the line through the DGL was first observed in the dual-polarization variables at 1730 UTC between 3.5 – 4.5 km MSL with K_{dp} > 0.8 ° km^{-1} and Z_{dr} > 1 dB in the upper part of the cloud (around 3.8 km or -13°C). Within the DGL, steady weak updrafts (< 1 m s^{-1}), associated with orographic lift similar to A', were observed (Fig. 10, Leg 8) between 1730-1742 UTC. Similar to A', Z_e remained between 0-9 dBZ_e at cloud top as B' passed through the ROD suggesting, together with the steady updraft shown in Fig. 10, continuous ice initiation. The snow associated with B' reached the ground about 36 min after seeding with Z_e > 5 dBZ_e, K_{dp} < 0.5 ° km^{-1}, and V_r of 1 m s^{-1} (Fig. 10) close to the surface (1-2 km AGL).

To further quantify these changes in microphysical processes, we conducted a quantitative analysis by calculating the mean values of dual-polarization parameters at each height and time step associated with A' (Fig. 11). Within the DGL (~3.3-4.1 km MSL), $\overline{Z_{dr}}$ steadily decreased from -0.2-0.6 dB at 4.1 km MSL (T = -15 °C) to -0.4-0 dB at 3.3 km MSL between 1705 to 1806 UTC. $\overline{K_{dp}}$ decreased only slightly within the DGL between 1705-1806 UTC from 0.5-0.6 ° km^{-1} at 4.1 km to 0.4-0.6 ° km^{-1} at 3.3 km. A peak in $\overline{K_{dp}}$ of 0.6 ° km^{-1} at 4 km MSL was observed between 1741-1753 UTC. $\overline{Z_e}$ increased below the DGL towards the surface to 10-15 dBZ_e most likely the result of aggregation and riming as snow fell towards the surface. A change towards more aggregated and rimed particles at the surface is seen in decreasing $\overline{\rho_{hv}}$ changing from 0.99 at 1705 UTC to 0.98 between 1734-1806 UTC but increased slightly afterwards. The enhanced snow growth, most likely related to riming, aggregation, and rapid dendritic growth above the higher terrain between 1718-1748 UTC, resulted in higher accumulated snowfall over the North Folk Range and Salmon River Mountains compared to the other areas downwind of PJ between 1705-1718 UTC (Fig. 3 in Friedrich et al. 2020).

4. Ice initiation and snow growth on 20 January

a. Natural cloud characteristics and atmospheric conditions

At cloud top (3.5-4 km), a neutral to slightly conditionally unstable atmosphere with -17 < T < -13 °C was observed (Fig. 3a, b). Predominantly southwesterly flow of < 10 m s^{-1} occurred up to 2.5 km changing to westerly flow between 2.5-6 km (Fig. 3c). Layers of wind shear > 0.02 s^{-1} were observed between 2-5 km MSL. The clouds formed principally over the higher terrain and did not extend far upwind of the mountain.

The UWKA flew a total of 10 legs, with seven flown in-cloud. The presence of extensive pockets of supercooled drizzle with D > 100 um, resulted in moderate icing conditions requiring that the UWKA fly three legs above cloud top. All in-cloud legs were within 1 km of cloud top at -11 < T < -14 °C. Leg-averaged, in-cloud LWCs ranged from 0.1 to 0.2 g m^{-3} with max LWC along a leg ranging from 0.45 to 0.6 g m^{-3}. Concentrations of cloud droplets were less than 30 cm^{-3}. Observed natural ice concentrations were generally less than 0.1 L^{-1} except in isolated pockets over higher terrain, where concentrations at flight level were between 1 and 5 L^{-1}.

b. Seeding operations and evolution of the seeding lines

The seeding aircraft flew eight legs (Legs A-H) on a constant flight track between 0003-0129 UTC at an altitude of 4.1 km for Legs A, F, and G, and 3.8 km for Legs B-E and H (Fig. 2). $\overline{LWC}$ between 0.04-0.28 g m^{-3} and $\overline{T}$ = -14°C were observed along nearly the entire seeding aircraft flight track during seeding Legs D, E, and H (Fig. 4b, Table 1). While Legs A, B, F, and G were flown mainly (89-100 % of the flight leg) above the cloud to avoid heavy icing, with $\overline{T}$ = -14 to -15°C, 59-82% of Legs C-D were also flown in cloud at T = -14°C, albeit with lower LWC values (0.11 < $\overline{LWC}$ < 0.18 g m^{-3}). As a result, only EJ flares were released during Legs A, F, G. BIP and EJ flares were used in Legs B-E, H (Table 1, Fig. 4b).

Reflectivity plumes from all eight seeding legs appeared as a zigzag seeding signature pattern of Lines A'-H' (Fig. 12, Movie 2). Background (natural) reflectivity values ranged between -30 to -10 dBZ_e throughout the event. A' and B' initially consisted of circular areas or "dots" of Z_e > 10 dBZ_e with background values of -30 to -5 dBZ_e and were first observed by the PJ DOW radar between 0030-0045 UTC ~5 km downwind of A-B at 2.6 km MSL (Movie 2). The Z_e dots were associated with ice particles forming from individual EJ flares deployed during A and the beginning of B (Fig. 4b). Their 3-4 km spacing matched the average 3 km distance between flare drops. As A' and B' moved downwind, C', D', and E' appeared between 0045-0124 UTC as semi-continuous lines, a result of continuous ejection of AgI through both BIP and EJ flares. F' and G' later appeared as Z_e dots between 0124-0143 UTC, the result of using only EJ flares along F and G. H', the final line, appeared between 0142-0152 UTC. As the lines propagated through the ROD, they broadened quickly and merged with other lines due to the low wind speed (< 10 m s^{-1}) and shear up to 0.02-0.03 s^{-1} between the surface and 4 km MSL. Precipitation accumulated mainly over the higher terrain and within the ROD (Fig. 3 in Friedrich et al. 2020).

The UWKA flew along the NW edge of seeding lines A'-H' and intersected the lines on their northernmost extent (Fig. 12) within a region of natural (background) Z_e between -15 and -10 dBZ_e (Fig. 13). Because lines A'-H' were arranged in a zigzag pattern, the UWKA intersections appeared as line pairs. Lines A'B' were first detected by the WCR at 0032 UTC during UWKA Leg 6, 3 km upwind of PJ and 21 min after seeding (Fig. 13). At this time, A'B' were confined to between 3-4 km MSL and were 1.5 km wide with a maximum Z_e of 0 dBZ_e. A'B' generated Z_e plumes that extended to the surface within 18 minutes (Fig. 13, Leg 7) and precipitated out (Fig. 13, Leg 8) 35 minutes after A'B' were first detected by the WCR. C'D' were detected by the WCR at 0047 UTC (Fig. 13, Leg 7), 15 minutes after the seeding aircraft turned from C to D. By 0108 UTC, Z_e plumes reached the surface. By Leg 9, C'D' were 8 km wide at 3.5 km MSL and contained Z_e of 10 dBZ$_e$ from cloud top to the surface. C'D' were still detectable during the UWKA's last leg (Fig. 13, Leg 10) but the maximum Z_e had decreased to 5 dBZ$_e$ and the width at 3.5 km narrowed to 2.5 km. E'-F' were not detected by the WCR during Leg 8 but were clearly visible on Leg 9, with Z_e plumes reaching the surface 20 minutes later on Leg 10. Similarly, G'H' were detected during UWKA Leg 9 at 0126 UTC, just 5 minutes after the seeding aircraft turned from Legs G-H. Z_e at this time was -10 to -5 dBZ$_e$ at 3.5 km MSL, only 5 dB greater than the natural cloud. Twenty-three minutes later (Fig. 13, Leg 10), Z_e within G'H' had increased to 5 dBZ$_e$, and extended from cloud top to 2 km MSL.

Lines A'B', C'D', E'F', and G'H' were detected by the WCR 30, 15, 30, and 5 minutes after seeding occurred, respectively. For A'B' and E'F', previous UWKA legs at 2 and 12 minutes after seeding, respectively, failed to detect a line. In all cases, lines were initially 1-2 km wide, and rapidly grew in width, with C'D' and E'F' achieving maximum width of 6-8 km 50-55 minutes after seeding. For C'D', E'F', and G'H', the seeding lines were discernible during the last leg flown by the UWKA (Fig. 13, Leg 10) from 0145 to 0149 UTC. Note also that the seeding lines drifted east of the UWKA flight track, since the UWKA flight track was not oriented directly along the mean wind (Fig. 2).

Based on the seeding aircraft track and the ambient winds, all seeding lines should have passed over PJ. The PJ MRR observed three distinct groups of seeding lines (Fig. 14). The first group between 0100 at 0114 UTC was related to C'D'. Lines E'F' and G'H' passed over the MRR between 0128-0131 UTC and 0154-0159 UTC, respectively. A maximum Z_e of 10 dBZ$_e$

and V_r = -1 m s^{-1} were observed. Based on both the MRR and WCR measurements, none of the snow generated by seeding reached the surface at PJ, but rather fell to the surface downwind.

c. Ice initiation and particle growth

The UWKA flew 5 legs (Legs 6-10) in which seeding lines were detected. Due to moderate icing conditions encountered on this day, only Legs 7, 9, and 10 were in-cloud while Legs 6 and 8 were above cloud. During the three in-cloud legs, three passes were made through lines C'D', two passes were made each through lines E'F' and G'H', and only one pass was made through lines A'B'. Passes through the seeding lines were made 5 to 75 minutes after seeding occurred and within 500 m of cloud top at the T = -12 °C level. Observed *LWC*s within the seeding lines ranged from < 0.01 to 0.143 g m^{-3} in C'D' (Fig. 15d), 0.01 to 0.047 g m^{-3} in E'F' (Fig. 15e), and 0.016 to 0.034 g m^{-3} in Line G'H' (Fig. 15f). For all particle size distributions measured at flight level within the seeding lines and 30 minutes or more after seeding, a distinctive "tail" of larger (ice) particles, D > 100 um, was evident with mean concentrations of 1 - 4 L^{-1} (Fig. 15a-c). In only two cases, in G'H' at 5 minutes after seeding and in C'D' at 15 minutes after seeding (Fig. 15a, Leg 7; Fig. 15c, Leg 9), was the tail absent, noting that during Leg 7 in C'D', 15 minutes after seeding, the UWKA passed underneath the level of the seeding line. The next *in-situ* observation of C'D' was not made until 60 minutes after seeding during Leg 9, by which time particles several mm in diameter were observed (Fig. 15a, Leg 9). In all cases, once ice formed, concentrations of ice particles with D > 100 um never exceeded 26 L^{-1} at flight level. Z_e at cloud top began to decrease with time, as the snow precipitated out of the cloud, despite that the clouds appeared to contain significant amounts of available SLW.

d. Snow growth and fallout

We were unable to analyze each seeding line separately in the PJ radar data as the eight seeding lines propagated slowly towards the northeast and started to merge quickly, in particular along the northern and southern turning points of the seeding aircraft (Fig. 16a). Instead, we divided the area that the seeding lines moved through into four northwest-southeast oriented, 8-km wide, and 60-km long boxes with Box 1 (Box 4) representing the earlier (later) stage of the seeding lines' evolution. Widespread snowfall over > 2,000 km^2, indicated by the area with Z_e > 15 dBZ$_e$ in Fig. 16b, was primarily observed in Box 2 and Box 3 between 2-3.5 km MSL between 0120-0215 UTC. The largest area of snowfall (> 3,000 km^2) was observed at 0123 UTC in Box 2 mainly associated with C'D' about 30-60 min after seeding (Fig. 16b). The largest area in Box 2 (> 3,000 km^2) was observed around 2.4-2.7 km MSL and was slightly higher, between 2.5-3 km MSL, in Box 3 (Fig. 16b). The decrease in area below 2.5 km MSL across all boxes was mainly related to complete and/or partial beam blockage of the radar beam, which was more severe with distance from the radar (particularly by Box 4) and, therefore, might not represent realistic snowfall conditions.

The magnitude of mean dual-polarization parameters ($\overline{Z_e}$, $\overline{K_{dp}}$, $\overline{Z_{dr}}$) indicate snow growth with time (Fig. 16 c-e). $\overline{Z_e}$ increased from ~10 dBZ$_e$ at 4 km to ~15 dBZ$_e$ at 2.5 km during the time of maximum snowfall (0100-0230 UTC). In addition, $\overline{Z_e}$ increased starting at 0034 UTC and peaked at around 15 dBZ$_e$ at and around 2.5 km between 0123-0151 UTC. Similar to $\overline{Z_e}$, $\overline{K_{dp}}$ showed very little temporal and vertical change. During the main snowfall, $\overline{K_{dp}}$ ranged between 0.3-0.5 ° km^{-1} with temporal variations of +- 0.1. A slight increase in $\overline{K_{dp}}$ within Box 2 and Box 3 occurred around 3.5 km MSL where T = -13 °C. This might be an indication of dendritic growth. Between 0100-0230 UTC, $\overline{Z_{dr}}$ remained slightly higher (0.5-1 dB) within the DGL (2.5-4 km MSL) compared to the surface. This indication of dendritic growth was consistently observed in Box 2 and Box 3 and sporadically in Box 1 and Box 4. As dendritic growth can lead to rapid snow formation and fallout, the question still remains why the seeding lines precipitated out so much faster and farther upwind compared to 19 Jan. This will be explored in section 6.

5. Ice initiation and snow growth on 31 January

a. Natural cloud characteristics and atmospheric conditions

Below 2.5 km, a stable boundary layer was observed with westerly winds > 8 m s^{-1} and T of about 0 °C (Fig. 3 a, b). Above this stable layer, westerly winds increased from 8 to 40 m s^{-1} at 5.5 km and above (Fig. 3c). Wind shear layers (> 0.03 s^{-1}) occurred between the surface and 5.5 km MSL. The atmosphere was stable with T decreasing from -5 °C at 2.5 km to -35 °C at 8 km.

Cloud tops with $-13 < T < -15$ °C were steady, between 4.8-5.2 km through the entire event, rarely varying more than a 100 m over a flight leg. The UWKA never penetrated more than 150 m below cloud top. Early legs identified severe icing conditions, with widespread presence of supercooled drops with D > 100 um and some observations of supercooled drops exceeding 150 µm in diameter. The limited *in-situ* observations on this day reveal near-cloud-top LWCs up to 0.4 g m^{-3} with droplet concentrations ranging from 20 to 30 cm^{-3}.

b. Seeding operations and evolution of the seeding lines

Due to severe icing and strong winds, the seeding aircraft only flew two legs (Legs A-B) deploying BIP and EJ flares continuously (Fig. 4c; Table 2) on a constant flight track between 2040-2105 UTC at 4.9 km MSL. Both legs were flown mainly in cloud (> 95%; Table 1) with westerly winds at about 30 m s^{-1} and $\bar{T}$ = -13 °C. LWC was < 0.5 g m^{-3} with $\overline{LWC}$ ranging between 0.23-0.24 g m^{-3} (Fig. 4c).

Two parallel lines, A' and A'', with Z_e > 15 dBZ_e (in a background of < 10 dBZ_e) separated by about 5 km emerged from the first seeding leg (Line A) at 2105 UTC, as observed by the DOW radars (Fig. 17, Table 1). A', farther downwind, had a more continuous pattern, consistent with the burning of BIP flares. A'', upwind of A', consisting of distinct comma-shaped areas of Z_e, related to individual EJ flares which dropped to lower altitudes into a weaker wind regime below the seeding aircraft flight level. The AgI from these EJ flares was vertically distributed over a depth of about 820 m below flight level, while BIP flares burned as a horizontal line at flight level. Considering shear of > 0.03 s^{-1} between 4.8-4.9 km MSL, AgI from BIP and EJ flares were advected at a different wind speed causing the separation into two parallel lines. A' (associated with BIPs) broadened rapidly from 3-5 km to > 10 km wide between 2114-2124 UTC (Fig. 18). A'' (associated with EJs) also broadened from < 1 km to about 5 km wide but remained much narrower than A'. Wind shear caused the upper part of A' and A'' to propagate faster than the lower part creating forward tilted seeding lines. A' reached the surface with Z_e > 15 dBZ_e at about 2114 UTC and continued to snow out mostly on the east side of the ROD (Friedrich et al. 2020). Areas with Z_e > 20 dBZ_e at the surface were still observed as A' moved out of the ROD (Figs. 17d, 18b). Snowfall with Z_e > 20 dBZ_e associated with A'' started to reach the surface at 2124 UTC.

The same pattern of two parallel lines of Z_e > 15 dBZ_e in a background of < 10 dBZ_e emerged after seeding Leg B. The northern part of B' and B" was first observed at 2122 UTC, with B' quickly merging with A" at 2129 UTC (Fig. 17c). At 2134 UTC, most of the lines had merged or had left the ROD.

c. Snow growth and fallout

The first seeding lines were observed about 30 minutes after seeding. Initially, echoes associated with EJ flares were smaller in size and occurred downwind of the BIP flares (Fig. 19a). Since both EJ and BIP flares merged within 10-15 minutes of radar detection and quickly moved out of the ROD, we analyzed spatiotemporal dual-polarization variables combined within both seeding legs. Dual-polarization variables indicated a rapid increase in snowfall and increase in the size of the seeding lines over 36 minutes. Below 3.5 km MSL, $\overline{Z_e}$ increased with time from ~7 dBZ_e at 2110 UTC up to 15 dBZ_e at 2134 UTC (Fig. 19b). Over the same time, $\overline{Z_e}$ between 4-4.5 km MSL increased from ~7 dBZ_e to 13 dBZ_e. Note that at and after 2134 UTC parts of the seeding lines already moved out of the ROD causing $\overline{Z_e}$ to decrease after 2134 UTC (Fig. 19b). An increase in $\overline{Z_e}$ with decreasing height was primarily observed after 2129 UTC indicating a rapid increase in particle diameter. Note that the increase in $\overline{Z_e}$ with decreasing height in Line A' was already observed at 2114 UTC and later occured persistently in all seeding lines (Fig. 18b). Little change in $\overline{Z_{dr}}$ with decreasing height was observed between 2117-2134 UTC; except for a slight increase in $\overline{Z_{dr}}$ of 0.3 dB with decreasing height at 2110 UTC (Fig. 19c). However, a peak in $\overline{Z_{dr}}$ was observed at 2141-2146 UTC at about 4.3 km (-13 °C) with an increase in $\overline{Z_e}$ below 4 km indicating the possibility of dendritic growth. While $\overline{K_{dp}}$ also remained relatively constant with decreasing height, a slight increase in $\overline{K_{dp}}$ was observed at 2110 and 2146 UTC in the DGL (Fig. 19d). $\overline{\rho_{hv}}$ profiles showed higher values at earlier (2110 UTC) and later times (2141-2146 UTC; Fig. 19e). All profiles showed a decrease of $\overline{\rho_{hv}}$ with decreasing height indicating a broadening of different hydrometeor types and shapes.

6. Influence of environmental conditions and seeding methods on snow amount and distribution

Friedrich et al. (2020) used a selection of reflectivity-snowfall relationships, precipitation gauge analysis, and the reflectivity fields discussed here to estimate total liquid equivalent snowfall (*LESnow*) for the three days. For more information on accuracy and range of snowfall estimates, we refer the reader to Friedrich et al. (2020). The largest amount of *LESnow* within the ROD was observed on 31 Jan with 339,540 m^3 over 2,410 km^2 following 19 minutes of seeding (Friedrich et al. 2020; Table 3). The second largest *LESnow*, 241,260 m^3 over 1,838 km^2 was on 20 Jan following 82 minutes of seeding. The smallest amount, 123,220 m^3 over 2,327 km^2, occurred on 19 Jan with 26 minutes of seeding (Friedrich et al. 2020). Snowfall on 19 Jan was distributed over the ROD with accumulations of 0.05 -0.14 mm. On 20 Jan snowfall mainly accumulated over an area 80% of the size of that on 19 Jan with accumulations of 0.05-1.5 mm (Fig. 3 in Friedrich et al. 2020). Snow accumulation on 31 Jan ranged between 0.05-0.25 mm. Seeding rates and amounts and environmental conditions must be responsible for how much (and whether or not) AgI is activated, how AgI and subsequent snowfall is transported and dispersed, and how it ultimately is distributed as snowfall on the mountains. Here, we consider what factors might have been responsible for the differences in total accumulation and spatial distribution in these three cases.

The three cases discussed here had similar cloud-top temperatures ranging from -13 to -15°C, natural ice particle concentrations of 1-5 L^{-1}, and cloud droplet concentrations < 30 cm^{-3} (Table 3). Differences were in the amount of AgI released, cloud-top altitude, *LWC* along and downwind of the seeding aircraft track, wind speed, and shear.

a. Impact of AgI amounts

Ice nucleation efficiency of AgI has been explored in experimental and theoretical studies (e.g., DeMott et al. 1983; DeMott 1994; Boe and DeMott 1999; Xue et al. 2013; Marcolli et al. 2016). Ice nucleus (IN) size and concentration has been identified as controlling ice formation, together with temperature, water vapor saturation, and cloud droplet, which will be discussed in the following sections. Particle size distribution generated by burning AgI flares depends on updraft strength with larger-sized particles occurring during weaker updrafts (DeMott et al. 1983). Since IN size and number concentration observations are not available, we chose to use the total AgI mass as a proxy ice nuclei production acknowledging that the same mass of AgI can lead to different size and number concentration under varying environmental conditions. Ultimately, the ice particle concentrations observed serves as a direct measure of how many ice nuclei actually activated within the seeding plumes.

A total of 445 g of AgI from EJ and BIP flares was released on 20 Jan from eight seeding legs over approximately 82 minutes, while on 19 and 31 Jan only 20% and 40% of the amount released on 20 Jan (87 and 178 g AgI), respectively, was distributed over two flight legs in about 19-26 min (Table 3). Despite releasing only 40% of the AgI on 31 Jan compared to 20 Jan, the amount of *LESnow* produced on 31 Jan was 29% more than was produced on 20 Jan. Further, the amount of *LESnow* produced on 20 Jan was only two times that amount produced on 19 Jan, despite releasing about five times more AgI. Clearly, more AgI did not necessarily produce more *LESnow* hinting that atmospheric conditions might play an essential role in the amount and distribution of snowfall. For 1 g of AgI released, 1,901 m^3 of total *LESnow* was generated on 31 Jan, 1,409 m^3 on 19 Jan, and 542 m^3 on 20 Jan. This implies that environmental conditions must have played an important role in the amount and distribution of snowfall produced through seeding.

b. Impact of LWC and T along the seeding track

Ice yield also depend temperature and LWC (e.g., DeMott et al. 1983; DeMott 1994; Boe and DeMott 1999; Xue et al. 2013; Marcolli et al. 2016). In a cloud chamber experiment, Boe and DeMott (1999) quantified the number of nuclei generated per gram of AgI as a function of temperature and LWC for BIP flares. In this experiment, the yield of ice crystals increases as T decreases from -5.5 to -10.2 degC with constant LWC. As T remains constant at -6 and -10 degC, more yield was found when LWC = 0.5 g m-3 rather than 1.5 g m-3.

T along the seeding track only fluctuated by 1-2degC between the days with -14degC during Legs A-B on 19 Jan, -15 to -14degC on 20 Jan, and -13degC on 31 Jan (Fig. 4). $\overline{LWC}$ > 0.23 g m^{-3} was observed along both seeding legs (A-B) on 31 Jan and two seeding legs (E, H) on 20 Jan, while all other in-cloud legs (A-D) on 20 Jan and every leg on 19 Jan had $\overline{LWC}$ ranging from 0.04 to 0.18 g m^{-3} (Table 1). Although the observations do not reveal information on how much AgI was activated, Legs D, E, H on 20 Jan had the highest measured $\overline{LWC}$ on that day and Lines D', E', H' showed higher Z_e values (peak at 30 dBZ$_e$) compared to A', B', and G' with Z_e peaks < 20 dBZ$_e$ (Fig. 12). Lines D', E', and H' also persisted longer (1-2 hrs) compared to the other lines on 20 Jan where snow fell out < 1 hr (Fig. 12). Lines D', E', and H' had higher total AgI discharge (> 63.2 g per leg) compared to other legs on this day (30.8-66.8 g), with the exception of C' which totaled 66.8 g of AgI. These observations are consistent in that lines with higher LWC and greater mass discharge of AgI persisted longer and with higher Z_e values than the other lines on this day.

On 31 Jan, the $\overline{LWC}$ was similar for both legs (0.24 and 0.23 g m^{-3} for Legs A and B, respectively). Also, for both legs the discharge of AgI was comparable (94.8 g compared to 83.8 g). The resulting seeding lines from BIP (A'-B') and EJ flares (A''-B'') had similar peak Z_e, respectively, with higher values associated with the BIP-related lines (30 dBZ$_e$ for A'-B' and 20 dBZ$_e$ for A''-B''). Seeding lines persisted as they both advected through the entire ROD. $\overline{LWC}$ for the two legs (A and B) on 19 Jan was 0.11 and 0.17 g m^{-3}. The amount of AgI released on these legs was nearly the same (44.8 and 42.6 g). Both legs had a similar maximum Z_e (30 dBZ$_e$) and persisted for a similar length of time (45 min).

Within a single day, our observations suggest that higher $\overline{LWC}$ along the seeding track and greater amounts of AgI release correspond to lines with greater Z_e that persist longer. However, this relationship does not necessarily hold when comparing across days. Lines associated with higher $\overline{LWC}$ along the seeding track (19 Jan: A-B; 20 Jan: C, D, E, H; 31 Jan: A-B) show similar peak Z_e of 30 dBZ$_e$. However, the width of the seeding line and the persistence within the ROD differs. The width of the seeding lines on 19 and 20 Jan are similar, while snow fell out rapidly over a smaller area producing 51% more snow on 20 Jan compared to 19 Jan (Fig. 3 in Friedrich et al. 2020). On 30 Jan, seeding lines were wider covering the largest areas (2,410 km^2) and the largest amount (339,540 m^3) of snowfall amongst the three cases. This implies that $\overline{LWC}$ along the seeding track plays an important role for ice initation and formation of the seeding lines. Yet, enhanced riming might determine how fast snow falls out and wind speed and shear determines AgI dissemination and transport across the ROD.

c. Impact of LWC downwind of the seeding track

While it is important to consider the amount of the *LWC along* the seeding track, one should also consider how the amount and persistence of *LWC downwind* of the seeding track may influence the evolution and persistence of seeding lines. The ability for the UWKA to obtain *in-situ* measurements downwind of the seeding track varied by day, due mainly to the presence of supercooled drizzle and its impact on airframe icing. On all three days, cloud droplet concentrations were < 30 cm^{-3} and mean cloud droplet diameters ranged from 20 to 30 μm (Table 3). UWKA-measured in-cloud $\overline{LWC}s$ were 0.1 - 0.2 g m^{-3} on all three days. However, on 31 Jan the UWKA conducted only a few flight legs in cloud, and those were always within 150 m of cloud top, while on 19 and 20 Jan, flight legs penetrated deeper into the cloud, typically 500 to 1000 m below cloud top. Maximum *LWCs* observed along legs were greatest on 20 Jan (0.45 - 0.6 g m^{-3}) and least on 19 Jan (0.3 - 0.4 g m^{-3}). From the UWKA measurements available from 31 Jan, *LWC*s appeared steadier through the length of the legs compared to 19 and 20 Jan.

On 19 Jan, supercooled drizzle drops were observed in isolated pockets and seldom exceeded 100 μm in diameter. On 20 Jan, drops with D < 150 μm were observed and occurred more extensively than on 19 Jan, often along ⅓ to ½ of a UWKA flight leg. The most supercooled drizzle was observed on 31 Jan. During the few cloud penetrations made by the UWKA, supercooled drizzle was widespread, with 100 < D < 200 μm.

Across the three days, the greatest amount of *LESnow* produced through seeding occurred on the day with the largest and most widespread occurrence of supercooled drizzle (31 Jan). One might conjecture that *LWC* was also more widespread on this day hence leading to greater drizzle production. However, the inability of the UWKA to penetrate more than 150 m below cloud top made comparison between days difficult. It is clear that the day with the least supercooled drizzle and the lowest *LWC* along the UWKA flight legs downwind of the seeding track (19 Jan) produced the smallest amount of *LESnow* through seeding.

d. Impact of wind shear

The question remains why 29% more total *LESnow* accumulated on 31 Jan compared to 20 Jan despite similar values of *LWC* and AgI released and why seeding lines precipitated out faster on 20 Jan compared to 19 Jan. Although the observations do not provide information on AgI dispersion and spatiotemporal AgI concentration, we hypothesize that strong shear leads to more efficient dispersion of AgI within supercooled clouds resulting in rapid and efficient precipitation formation, which can be tested in future modeling work. Shear at and below seeding level was ~0.01 s^{-1} greater on 20 and 31 Jan compared to 19 Jan (Table 3) resulting in more efficient dispersion of AgI. In particular, the rapid decrease in wind speed with decreasing height (40-30 m s^{-1} between 4-5 km) on 31 Jan led to a separation of the BIP and EJ flares, which was not observed on 19 and 20 Jan. This separation of flares shown in the Z_e fields further suggested that AgI was activated and distributed over a much larger area (Figs. 17, 18) compared to 19 and 20 Jan (Figs. 5-6, 12-13). The efficient AgI dispersion on 31 Jan, in combination with greater *LWC* along and downwind of the seeding track and most supercooled drizzle observed, contributed to the largest area covered by snowfall (2,410 km^2), highest peak snowfall at 0.25 mm, and highest total accumulations 339,540 km^2 on 31 Jan compared to 19 and 20 Jan (1,838-2,327 km^2; 0.14-1.5 mm; 123,220-241,260 m^3; Table 3). Interestingly, on 31 Jan, reflectivity plumes associated with BIP flares resulted in qualitative larger seeded areas (larger area of $Z_e > 0$ dBZ_e) compared to EJ flares (Fig. 18).

e. Impact of wind speed

While shear affects AgI dispersion, stronger winds will transport ice particles produced through seeding farther downwind. Winds at the seeding level were strongest on 31 Jan, with seeding lines remaining only 30 min in the ROD, with not all snow reaching the surface inside the ROD. Conversely, winds were weakest on 20 Jan and on this day the seeding lines mostly reached the surface within the ROD, approximately within 40 km downwind of the seeding legs. On 19 Jan, winds were 5 - 8 m s^{-1} stronger than on 20 Jan and 12 to 25 m s^{-1} weaker than on 31 Jan. *LESnow* on 19 Jan was almost equally distributed over the ROD, while on 20 Jan snowfall mainly accumulated over an area half the size of that on 19 Jan (Fig. 3 in Friedrich et al. 2020). Wind speed, therefore, played a role in the residence time of seeding lines within the ROD and the resultant distribution of snowfall.

f. Impact of ice particle growth mechanisms

In-situ observations of crystal concentrations and habits were made on both 19 and 20 Jan. On both days, the approximate time between the release of AgI and the development of a seeding line with Z_e > 5 dBZ_e was 15 to 30 minutes. After seeding lines were detected by the UWKA, ice particle concentrations remained, on average, between 2.5 - 8 L^{-1} on 19 Jan and slightly less (1 - 3.8 L^{-1}) on 20 Jan. Also, IWC within seeding lines ranged from 0.1 - 0.48 g m^{-3} on 19 Jan and 0.1 - 0.27 g m^{-3} on 20 Jan. Despite these lower values on 20 Jan, more *LESnow* was produced and the lines precipitated out faster on this day.

As noted earlier, *LWC* measured by the UWKA was greater on 20 Jan and supercooled drizzle was more prevalent. This may have resulted in more riming. Indeed, images of ice crystals from the UWKA suggest this to be the case, leading to more rapid fallout. Unlike 20 Jan, the radar returns on 19 Jan persistently maintained strong echoes ($Z_e > 5$ dBZ$_e$) near cloud top. Evidence of dendritic growth in the upper part of the cloud was continuously observed as the seeding lines passed through the ROD. We hypothesize that ice initiation continuously occurred as unactivated residual AgI was transported farther downwind and updrafts, associated with encountering higher terrain, provided *SLW* due to local orographic ascent. This likely aided in the persistence of the seeding lines on 19 Jan compared to 20 Jan.

g. **Impact of snow growth mechanisms**

Snow growth mechanisms were similar for all three cases. Dendritic growth was observed in the upper part of the clouds where $-10 < T$ -15°C as the seeding lines passed through the ROD. Snow growth related to riming and aggregation occurred closer to the surface, based on radar polarization signatures. The largest increase in Z_e with decreasing height was observed on 31 Jan (6.25 dBZ$_e$ over 1 km), the day with the greater *LWC* along and downwind of the seeding track, most supercooled drizzle, and the largest *LESnow*. On 20 Jan, Z_e increased by 4.6 dBZ$_e$ over 1 km with decreasing height, while 3 dBZ$_e$ over 1 km was observed on 19 Jan. These increases occurred close to the surface below the dendritic growth zone. Snowfall at the surface was first observed 12 min after seeding on 31 Jan and 40-45 min on 19 and 20 Jan (Table 3; Friedrich et al. 2020). Rapid fallout of snow, highest *LWC*, and highest Z_e gradient led to the conclusion that heavy riming must have occurred on 31 Jan. Riming most likely also occurred on 19 and 20 Jan, but to a lesser degree. Comparing 19 and 20 Jan, snow fell out faster on 20 Jan, the day with higher *LWC*, extensive regions of supercooled drizzle droplets with $50 < D < 150$ um, and more AgI release (445 g vs. 87.4 g).

Cloud-top heights were the highest on 31 Jan and lowest on 19 Jan (Table 2). The primary impact of cloud top height is to affect the residence time of snow in the air prior to impacting the mountain when seeding is conducted near the cloud top. Given similar winds, longer residence times shift the snow further downwind across the target area.

7. Conclusion

Ice and snow production and microphysical processes for three airborne cloud seeding events with well-defined, traceable plumes of enhanced reflectivity were quantified and environmental conditions were studied using airborne and ground-based remote sensing and *in-situ* observations. Figure 20 summarizes the evolution of the seeding lines and the distribution of snowfall during the three cases discussed here. As AgI interacted with the SLW cloud, droplets started to freeze and continued to growth first through deposition and then through riming and aggregation. Wind shear resulted in vertical tilt of the seeding lines. During weak wind conditions (Fig. 20a; 19 and 20 Jan), rapid growth caused snow falling out 40-45 min after seeding with the heaviest snow accumulating 10-30 km downwind of the seeding track (Friedrich et al. 2020). During snow growth, Z_e generally increased with decreasing height. However, along some seeding segments on 19 Jan, Z_e remained enhanced near cloud top. It is hypothesized that ice initiation continuously occurred as unactivated residual AgI was transported farther downward and updrafts, associated with higher terrain, provided *SLW* during local orographic ascent. As a result, snow was more equally distributed downwind of the seeding tack on 19 Jan compared to 20 Jan. During strong wind conditions (Fig. 20b; 31 Jan), snow fell out 12 min after seeding but was transported farther downwind with the heaviest snow accumulating beyond 20 km downwind. Between the three cases, the largest amount of *LESnow* was observed on 31 January.

The distribution and amount of snowfall was also linked to the amount of AgI released and the temporal and spatial evolution of atmospheric variables. While the experimental design, cloud-top temperatures, natural ice particle concentrations, and cloud droplet concentrations were similar during the three seeding events, the amount of AgI released, wind speed and shear, *LWC* along and downwind of the seeding track, and the presence of supercooled drizzle drops differed. The findings from this study can be summarized as followed:

- More AgI did not necessarily produce more liquid equivalent snowfall (*LESnow*). The day (20 Jan) with the most AgI released (445 g) only produced the second greatest amount of total *LESnow* (241,260 m^{-3}).
- *LWC* along the seeding track plays an important role for ice initiation and formation of the seeding lines. Seeding legs with $\overline{LWC}$ > 0.23 g m^{-3} and greater amounts of AgI release (> 63.2 g per leg) correspond to lines with greater Z_e (peak at 30 dBZ_e).
- The greatest amount of *LESnow* produced through seeding occurred on the day (31 Jan) with the largest and most widespread occurrence of supercooled drizzle and largest amount of *LWC* downwind of the seeding track (Fig. 20b).
- Wind speed and shear determines AgI dissemination and transport. The day (31 Jan) with the strongest wind shear produced the greatest amount of *LESnow*. The stronger the wind, the farther away the snowfall occurs from the seeding track (Fig. 20).
- Degree of riming determines how fast snow falls out. Snow fell out within 15 to 40 min on days (20 and 31 Jan) with greater *LWC* along and downwind of the seeding track, and widespread occurrence of supercooled drizzle.

In summary, the greatest amount of *LESnow*, largest area covered by snowfall, and highest peak snowfall produced through seeding occurred on the day (31 Jan) with the largest and most widespread occurrence of supercooled drizzle, highest wind shear, and greater LWC along and downwind of the seeding track. The day (19 Jan) with the least supercooled drizzle and the lowest LWC along the UWKA flight legs downwind of the seeding track produced the smallest amount of *LESnow* through seeding.

The results from this study provide a first step towards answering the question about how environmental conditions and amount of AgI affect cloud seeding efficacy. This study, in concert with Friedrich et al. (2020) and French et al. (2018), provides a comprehensive analysis of cloud seeding efficacy for the three cloud seeding events. These findings set a stage for analyzing microphysical and dynamical conditions during other cloud seeding events observed during SNOWIE as well as validating numerical models that simulate the microphysical impacts of cloud seeding and improving interpretation of precipitation observations during cloud seeding operations. Results can guide process modeling studies focusing on the role of atmospheric conditions and AgI amount and dispersion. Numerical modeling can also be used to explore a quantitative link between the environmental parameters, cloud and precipitation properties, AgI amount, and snowfall amount and distribution.

Acknowledgments: We would like to thank the crews from the University of Wyoming King Air (UWKA) and Doppler on Wheels (DOW) radars from the CSWR as well as all students from the Universities of Colorado, Wyoming, and Illinois for their help operating and deploying instruments during the campaign. Funding for CSWR-DOWs and the UWKA was provided through the National Science Foundation (NSF) awards AGS-1361237 and AGS-1441831, respectively. Funding for seeding aircraft was provided by Idaho Power Company. The research was supported under NSF Grants AGS-1547101, AGS-1546963, AGS-1546939, AGS-2016106, AGS-2015829, and AGS-2016077. This material is based upon work supported by the National Center for Atmospheric Research, which is a major facility sponsored by the National Science Foundation under Cooperative Agreement No. 1852977.

Data Availability Statement: All data presented here are publicly available through the SNOWIE data archive website (https://data.eol.ucar.edu/master_lists/generated/snowie/) maintained by the Earth Observing Laboratory (EOL) at the National Center for Atmospheric Research (NCAR) and the SNOWIE radar data archive (ftp://snowiepi:cswrsnowie@cswrdata.org) maintained by the Center for Severe Weather Research (CSWR).

Appendix A

Observing systems and data processing

a. Aircraft operations and instruments

The seeding aircraft released burn-in-place (BIP) and ejectable (EJ) flares of AgI and provided flight-level measurements of temperature and cloud liquid water content along its track (Table 1 in Tessendorf et al. 2019). Each seeding leg (solid lines in Fig. 2) was oriented perpendicular to the mean wind direction at flight level and was flown upwind of the ground-based radars. Seeding legs were repeated 2 - 8 times during a flight. When in cloud, the seeding aircraft released AgI with both BIP and EJ flares. The amount of AgI released during each leg is listed in Table 1. Only EJ flares were used during legs that occurred above clouds.

Detailed measurements of cloud microphysical structure were provided by instruments mounted onboard the University of Wyoming King Air (UWKA) research aircraft (Rodi 2011). The UWKA flew tracks prior to, during, and after cloud seeding. The tracks were flown along the direction of the mean wind perpendicular to the seeding aircraft legs, and passed over the radar at the Packer John instrument site (dashed lines in Fig. 2). Typically, the UWKA repeated 10 flight legs over a 4-hour flight period, with two to four legs completed prior to the start of seeding. Legs were repeated on the same track for a given flight, but tracks were rotated flight to flight, depending on wind direction. If cloud conditions allowed, the UWKA flew within the cloud, at or below the altitude at which the seeding material was released. On 19 January, all flight legs were flown below the cloud top; while on 20 January four of the ten flight legs were above cloud top due to moderate icing conditions. On 31 January, due to severe icing, all legs were flown above cloud top. Therefore, remote sensing observations from the UWKA were available for all three days, while *in-situ* measurements were available on two days.

Vertical cross-sections of equivalent radar reflectivity factor (Z_e) and vertical Doppler radial velocity (V_r) along the UWKA flight track were provided by the Wyoming Cloud Radar (WCR), a W-band radar on the UWKA (Wang et al. 2012). The WCR has a minimum detectable signal of -40 dBZ_e at 1 km and was able to detect liquid cloud hydrometeors in the absence of ice and precipitation in the SNOWIE clouds. V_r measurements were calibrated and corrected for aircraft motion following Haimov and Rodi (2013). The WCR provides a ~30 m (along beam, vertical) and ~15 m (along track; horizontal at 1 km) resolution.

An array of *in-situ* instruments measured cloud dynamical, thermodynamical, and microphysical parameters along the flight track of the UWKA. Tessendorf et al. (2019) list the instruments on the UWKA. Here, we briefly describe those relevant to this study. Details of processing and related uncertainties are presented in the supplementary information in French et al. (2018). Bulk cloud water and ice mass was provided by a deep-cone Nevzorov probe mounted on the nose of the UWKA (Korovlev et al. 2013). The methodology for calibrating and retrieving the liquid and ice water content from the Nevzorov probe on the UWKA is discussed in Faber et al. (2018). Hydrometeor size distributions were compiled from data collected from three optical probes: a cloud droplet probe (CDP; Lance et al. 2010; Faber et al. 2018), a two-dimensional stereo probe (2DS; Lawson et al. 2006), and a two-dimensional precipitation probe (2DP; Knollenberg 1981; Baumgardner et al. 2017). Distributions were computed for hydrometeors with diameters ranging from 2 um to several mm. For particles with diameters larger than 50 um, two-dimensional images were captured that were used to identify particle type and phase.

b. Ground-based radars

Two dual-polarization scanning X-band Doppler On Wheels (DOW; Wurman 2001) radars were deployed, one at Packer John (PJ; 2138 m MSL) and the other at Snowbank (SB; 2503 m MSL; Fig. 2) ridgetop sites. The range resolution was 50 m and the maximum range 50 km (gray shaded area in Fig. 2). DOW radars provided V_r, Z_e, differential reflectivity (Z_{dr}), special differential phase (K_{dp}), and correlation coefficient (ρ_{hv}). The scan strategy for both radars is shown in Table 2. Friedrich et al. (2020) provide information on quality control, calibration, and ground clutter removal. The raw data were converted to quality-controlled volumetric data in Cartesian coordinates at 100 m horizontal and 250 m vertical resolution for 19 and 31 Jan from the SB radar and for 20 Jan from the PJ radar. Seeding lines were isolated from the background precipitation through manual identification and masking of the surrounding Z_e. To further reduce the influence of natural precipitation surrounding the seeding lines, seeding lines were defined by isolating areas of $Z_e > 10$ dBZ$_e$. Mean dual-polarization parameters were derived as a function of height for individual seeding lines (19 Jan), regions containing seeding lines (20 Jan), or a combination of all seeding lines (31 Jan).

In addition to the two scanning radars, a vertically pointing Ka-band METEK Micro Rain Radar (MRR; Peters et al. 2002) was deployed at PJ. The instrument operated in a continuous wave mode at 24.23 GHz providing vertical profiles of Z_e, V_r, and spectral width at a vertical resolution of 100 m up to 5.2 km MSL (31 range gates). Data were averaged over 1-min intervals. A Doppler spectra post-processing technique (Maahn and Kollias 2012) was implemented to improve sensitivity for snow and to de-alias Doppler velocities so that vertical particle motions could be distinguished within ± 12 m s^{-1}. The first two range gates were unreliable and removed in this post-processing.

Appendix B

List of Appreciations

AgI – silver iodide

BIP - Burn-In-Place

D – diameter

DGL - Dendritic Growth Layer

DOW – Doppler On Wheels

EJ – EJectable

IWC - Ice Water Content

K_{dp} - special differential phase

LESnow - Liquid Equivalent Snowfall

LWC – Liquid Water Content

MRR – Micro Rain Radar

PJ – Packer John site

ROD – Radar Observational Domain

SB – SnowBank site

SLW - Supercooled Liquid Water

SNOWIE - Seeded and Natural Orographic Wintertime Clouds: The Idaho Experiment

T - Temperature

UWKA - University of Wyoming King Air

V_r – radial velocity

WCR – Wyoming Cloud Radar

Z_{dr} - Differential reflectivity

Z_e - Radar reflectivity factor

ρ_{hv} - Correlation coefficient

References

Andrić, J., M. Kumjian, D. Zrnić, J. Straka, and V. Melnikov, 2013: Polarimetric signatures above the melting layer in winter storms: An observational and modeling study. J. Appl. Meteor. Climatol., 52, 682–700.

Baumgardner, D., and Coauthors, 2017: Cloud ice properties: In situ measurement challenges. *Meteorological Monographs*, **58**, 9.1–9.23, doi:10.1175/AMSMONOGRAPHS-D-16-0011.1.

Bechini, R., L. Baldini, and V. Chandrasekar, 2013: Polarimetric radar observations in the ice region of precipitating clouds at C-band and X-band radar frequencies. J. Appl. Meteor. Climatol., 52, 1147–1169.

Boe, B. A., and P. J. DeMott, 1999: Comparisons of Lohse wing-tip generators and burn-in-place pyrotechnics in the North Dakota cloud modification project. *J. Weather Modification*, **31**, 109-118.

Cober, S. G., J. W. Strapp, and G. A. Isaac, 1996: An example of supercooled drizzle drops formed through a collision–coalescence process. J. Appl. Meteor., 35, 2250–2260.

DeMott, P. J., 1995: Quantitative description of ice formation mechanisms of silver iodide-type aerosols. Atmospheric Research, 38, 63-99.

DeMott, P. J., W. G. Finnegan, and L. O. Grant, 1983: An application of chemical kinetic theory and methodology to characterize the ice nucleation properties of aerosols used for weather modification. J. Appl. Meteor., 22, 1190-1203.

Deshler, T., and D. W. Reynolds, 1990: The persistence of seeding effects in a winter orographic cloud seeded with silver iodide burned in acetone. J. Appl. Meteor., 29, 477–488, https://doi.org/10.1175/1520-0450(1990)029<0477:TPOSEI>2.0.CO;2.

Deshler, T., D. W. Reynolds, and A. W. Huggins, 1990: Physical response of winter orographic clouds over the Sierra Nevada to airborne seeding using dry ice or silver iodide. J. Appl. Meteor., 29, 288–330, https://doi.org/10.1175/1520-0450(1990)029<0288:PROWOC>2.0.CO;2.

Faber, S., J. R. French, and R. Jackson, 2018: Laboratory and in-flight evaluation of measurement uncertainties from a commercial Cloud Droplet Probe (CDP). *Atmospheric Measurement Techniques*, **11**, 3645–3659, doi:10.5194/amt-11-3645-2018.

Field, P. R., and A. J. Heymsfield, 2003: Aggregation and scaling of ice crystal size distributions, *Journal of the Atmospheric Sciences*, **60**, 544-560.

French, J. R., K. Friedrich, S. Tessendorf, R. Rauber, B. Geerts, R. Rasmussen, L. Xue, M. Kinkel, and D, Blestrud, 2018: Precipitation formation from orographic cloud seeding. Proceedings of the National Academy of Sciences of the United States of America. 201716995; DOI: 10.1073/pnas.171699511.

Friedrich, K., K. Ikeda, S. A. Tessendorf, J. R. French, R. M. Rauber, B. Geerts, L. Xue, R. M. Rasmussen, D. R. Blestrud, M. L. Kunkel, N. Dawson, and S. Parkinson, 2020: Quantifying snowfall from orographic cloud seeding. Proceedings of the National Academy of Sciences of the United States of America. 201917204; DOI: 10.1073/pnas.1917204117

Fukuta, N., and T. Takahashi, 1999: The growth of atmospheric ice crystals: A summary of findings in vertical supercooled cloud tunnel studies. J. Atmos. Sci., 56, 1963–1979.

Geerts, B., Q. Miao, Y. Yang, R. Rasmussen, and D. Breed, 2010: An airborne profiling radar study of the impact of glaciogenic cloud seeding on snowfall from winter orographic clouds. J. Atmos. Sci., 67, 3286–3302.

Geerts, B. and co-authors, 2013: The AgI Seeding Cloud Impact Investigation (ASCII) campaign 2012: overview and preliminary results. J. Wea. Mod., 45, 24-43.

Geresdi, I., R. M. Rasmussen, and W. Grabowski, 2005: Sensitivity of freezing drizzle formation in stably stratified clouds to ice processes. Meteor. Atmos. Phys., 88, 91–105.

Grazioli, J., G. Lloyd, L. Panziera, C. Hoyle, P. Connoly, J. Henneberger et al., 2015: Polarimetric radar and in situ observations of riming and snowfall microphysics during CLACE 2014. Atmospheric Chemistry and Physics, 15, 13787–13802.

Griffin, E., T. Schuur, and A. Ryzhkov, 2018: A polarimetric analysis of ice microphysical processes in snow, using quasi-vertical profiles. J. Appl. Meteor. Climatol., 57, 31–50.

Haimov, S. and A. Rodi, 2013: Fixed-Antenna Pointing-Angle Calibration of Airborne Doppler Cloud Radar. J. Atmos. Oceanic Technol., 30, 2320–2335.

Harimaya, T., and M. Sato, 1989: Measurement of the riming amount on snowflakes, J. Fac. Sci. Hokkaido Univ., 8(4), 355–366.

Hobbs, P. V., 1975: The nature of winter clouds and precipitation in the Cascade Mountains and their modification by artificial seeding. Part III: Case studies of the effects of seeding. J. Appl. Meteor., 14, 819–858, https://doi.org/10.1175/1520-0450(1975)014<0819:TNOWCA>2.0.CO;2.

Hobbs, P. V., J. H. Lyons, J. D. Locatelli, K. R. Biswas, L. F. Radke, R. R. Weiss Sr., and A. L. Rangno, 1981: Radar detection of cloud-seeding effects. Science, 213, 1250–1252, https://doi.org/10.1126/science.213.4513.1250.

Hogan, R. J., P. R. Field, A. J. Illingworth, R. J. Cotton, and T. W. Choularton, 2002: Properties of embedded convection in warm-frontal mixed-phase cloud from aircraft and polarimetric radar. Q.J.R. Meteorol. Soc., 128: 451-476. doi:10.1256/003590002321042054

Ikeda, K., R. M. Rasmussen, W. D. Hall, and G. Thompson, 2007: Observations of freezing drizzle in extratropical cyclonic storms during IMPROVE-2. J. Atmos. Sci., 64, 3016–3043

Kennedy, P. C. and S. A. Rutledge 2011: S-band dual-polarization radar observations of winter storms. J. Appl. Meteor. Climatol., 50, 844–858.

Knollenberg, R. G., 1981: Technique for probing cloud microstructure. *Clouds, Their Formation, Optical Properties, and Effects,* eds Hobbs PV, Deepak A. Academic Press, New York, p 15-91.

Korolev, A., J. W. Strapp, G. A. Isaac, and E. Emery, 2013: Improved airborne hot-wire measurements of ice water content in clouds. *J. Atmos. Ocean. Tech*, **30**, 2121–2131, doi:10.1175/JTECH-D-13-00007.1.

Lamb, D., and J. Verlinde, 2011: Physics and chemistry of clouds. p. 584. Cambridge, UK: Cambridge University Press.

Lance, S., C. A. Brock, D. Rogers, and J. A. Gordon, 2010: Water droplet calibration of the Cloud Droplet Probe (CDP) and in-flight performance in liquid, ice and mixed-phase clouds during ARCPAC. *Atmospheric Measurement Techniques*, **3**, 1683–1706, doi:10.5194/amt-3-1683-2010.

Lawson, R. P., P. Zmarzly, K. Weaver, Q. Mo, D. O'Connor, B. Baker, and H. Jonsson, 2006: The 2D-S (Stereo) orobe: Design and preliminary tests of a new airborne, high-speed, high-resolution particle imaging probe. *J. Atmos. Ocean. Tech*, **23**, 1462–1477, doi:10.1175/jtech1927.1.

Ludlam, F. H., 1955: Artificial snowfall from mountain clouds, Tellus, 7:3, 277-290, DOI: 10.3402/tellusa.v7i3.8908

Maahn, M. and P. Kollias, 2012: Improved Mirco Rain Radar snow measurements using Doppler spectra post-processing. Atmos. Meas. Tech., 5, 2661-2673.

Majewski, A., and J. French, 2020: Supercooled drizzle development in response to semi-coherent vertical velocity fluctuations within an orographic layer cloud. *Atmos. Chem. Phys.,* In Press.

Marcolli, C., B. Nagare, A. Welti, and U. Lohmann, 2016: Ice nucleation efficiency of AgI: review and new insights. Atmos. Chem. Phys. 16, 8915-8937.

Mitchell, D. L., R. Zhang, and R. L. Pitter, 1990: Mass-dimensional relationships for ice particles and the influence of riming on snowfall rates, J. Appl. Meteor., 29(2), 153–163.

Moisseev, D., E. Saltikoff, and M. Leskinen, 2009: Using dual-polarization weather radar observations to improve quantitative precipitation estimation in snowfall. Proceedings of the 8th International Symposium on Tropospheric Profiling, A. Apituley, H. W. J. Russchenberg, and W. A. A. Monna, Eds., Royal Netherlands Meteorological Institute, S11-O04. [Available online at http://cerberus.rivm.nl/ISTP/data/1712984.pdf.]

Moisseev, D., S. Lautaportti, J. Tyynela, and S. Lim, 2016: Dual-polarization radar signatures in snowstorms: Role of snowflake aggregation. J. Geophys. Res., 121, 12644–12655.

Moisseev, D., A. von Lerber, and J. Tiira, 2017: Quantifying the effect of riming on snowfall using ground-based observations. J. Geophys. Res., 122, 4019–4037.

Murakami, M., Y. Yamada, T. Matsuo, H. Mizuno, and K. Morikawa, 1992: Microphysical structures of warm-frontal clouds. The 20 June 1987 case study. J. Meteor. Soc. Japan, 70, 877–895.

Peters G., B. Fischer, and T. Andersson, 2002: Rain observations with a vertically looking Micro Rain Radar (MRR). Boreal Env. Res., 7, 353-362.

Pokharel, B., B. Geerts, X. Jing, K. Friedrich, J. Aikins, D. Breed, R. Rasmussen, and A. Huggins, 2014: The impact of ground-based glaciogenic seeding on clouds and precipitation over mountains: a multi-sensor case study of shallow precipitating orographic cumuli. Atmos. Res., 147, 162-182. http://dx.doi.org/10.1016/j.atmosres.2014.05.014

Pokharel, B., B. Geerts, X. Jing, K. Friedrich, K. Ikeda, and R. Rasmussen, 2017: A multi-sensor study of the impact of ground-based glaciogenic seeding on clouds and precipitation over mountains in Wyoming. Part II: Seeding impact analysis. Atmos. Res., 183, 42–57.

Politovich, M. K., 1989: Aircraft icing caused by large supercooled droplets. J. Appl. Meteor., 28, 856–868.

Pruppacher, H. R. and Klett, J. D., 1997: Microphysics of clouds and precipitation. 2nd Edition, Kluwer Academic, Dordrecht, 954 p.

Rangno, A. L., and P. V. Hobbs, 1991: Ice particle concentrations and precipitation development in small polar maritime cumuliform clouds. Quart. J. Roy. Meteor. Soc., 117, 207–241.

Rasmussen, R. M., B. C. Bernstein, M. Murakami, G. Stossmeister, and B. Stankov, 1995: The 1990 Valentine's Day arctic outbreak. Part I: Mesoscale and microscale structure and evolution of a Colorado Front Range shallow upslope cloud. J. Appl. Meteor., 34, 1481–1511.

Rauber, R. M., L. O. Grant, D.-X. Feng, and J. B. Snider, 1986: The characteristics and distribution of cloud water over the mountains of northern Colorado during wintertime storms. Part I: Temporal variations. J. Climate Appl. Meteor., 25, 468–488, https://doi.org/10.1175/1520-0450(1986)025,0468:TCADOC.2.0.CO;2.

Rauber, R. M.., B. Geerts, L. Xue, J. French, K. Friedrich, R. Rasmussen, S. Tessendorf, D. Blestrud, M. Kunkel, S. Parkinson, 2019: Wintertime orographic cloud seeding - A review. J. Appl. Meteor. Climatol., 58, 2117-2140.

Reinking, R. F., 1979: The onset and early growth of snow crystals by accretion of droplets. J. Atmos. Sci., 36, 870–881, https://doi.org/ 10.1175/1520-0469(1979)036,0870:TOAEGO.2.0.CO;2.

Rodi, A., 2011: King of the Air: The evolution and capabilities of Wyoming's observation aircraft. *Meterol. Technol. Int.*, May 2011: 44-47.

Ryzhkov, A. V., and D. S. Zrnic, 1998: Discrimination between rain and snow with a polarimetric radar. J. Appl. Meteor., 37, 1228–1240.

Schneebeli, M., N. Dawes, M. Lehning, and A. Berne, 2013: High-resolution vertical profiles of X-Band polarimetric radar observables during snowfall in the Swiss Alps. J. Appl. Meteor. Climatol., 52, 378–394, https://doi.org/10.1175/JAMC-D-12-015.1.

Schrom, R. S., M. R. Kumjian, and Y. Lu, 2015: Polarimetric radar signatures of dendritic growth zones within Colorado winter storms. J. Appl. Meteor. Climatol., 54, 2365–2388.

Takahashi, T., T. Endoh, G. Wakaham, and N. Fukuta, 1991: Vapor diffusional growth of freefalling snow crystals between -3 and -23C. Journal of the Meteorological Society of Japan, 69, 15–30.

Tessendorf, S. A., J. R. French, K. Friedrich, B. Geerts, R. M. Rauber, R. M. Rasmussen, L. Xue, K. Ikeda, D. R. Blestrud, M. L. Kinkel, S. Parkinson, J. S. Snider, J. Aikins, S. Faber, A. Majewski, C. Grasmick, P. T. Bergmaier, A. Janiszeski, A. Springer, C. Weeks, D. J. Serke, R. Bruintjes, 2019: A transformational approach to winter orographic weather modification research: The SNOWIE Project. Bull. Meteor. Soc., 96, 2195–2198, https://journals.ametsoc.org/doi/10.1175/BAMS-D-17-0152.1

Williams, E., D. Smalley, M. Donovan, R. Hallowell, K. Hood, B. Bennett, B. et al., 2015: Measurements of differential reflectivity in snowstorms and warm season stratiform systems. J. Appl. Meteor. Climatol., 54, 573–595.

Wang, Z., and Coauthors, 2012: Single Aircraft Integration of Remote Sensing and in Situ Sampling for the Study of Cloud Microphysics and Dynamics. *Bull. Amer. Meteor. Soc*, **93**, 653–668, doi:10.1175/BAMS-D-11-00044.1.

Wurman, J., 2001: The DOW mobile multiple-Doppler network. Preprints, 30th Int. Conf. on Radar Meteorology, Munich, Germany, Amer. Meteor. Soc., 95–97.

Xue, L., and Coauthors, 2013: Implementation of a silver iodide cloud seeding parameterization in WRF. Part I: Model description and idealized 2D sensitivity tests. J. Appl. Meteor. Climatol., 52, 1433–1457, https://doi.org/10.1175/JAMC-D-12-0148.1.

Tables

Table 1: Number of burn-in-place (BIP) and ejectable (EJ) flares, amount of AgI released, mean LWC along each seeding leg, and percentage of the flight leg conducted in clouds. The BIP (EJ) flares burn for about 4.5 min (35 s) and release 16.2 g (2.2 g) of AgI per flare. The flares produce a horizontal (vertical) line of AgI of about 35 km (820 m) along (below) flight level resulting in a concentration of about 0.5 g km^{-1} (2.7 g km^{-1}) of BIP-AgI (EJ-AgI) flares along (below) the flight track. The seeding aircraft, flying at a speed of about 130 m s^{-1}, released BIP and EJ flares as shown in Fig. 3.

	EJ		**BIP**		**Total**	**LWC**	**In-cloud**
	# of flares	AgI (g)	# of flares	AgI (g)	AgI (g)	Mean (g m^{-3})	%
19 Jan							
Leg A	13	28.6	1	16.2	44.8	0.17	52
Leg B	12	26.4	1	16.2	42.6	0.11	66
Total A-B	**25**	**55**	**2**	**32.4**	**87.4**		
Leg C	16	35.2	2	32.4	67.6	0.09	47
Leg D	15	33	1	16.2	49.2	0.08	40
Leg E	18	39.6	1	16.2	55.8	0.08	14
Leg F	19	41.8	2	32.4	74.2	N/A	0

Total A-F	**118**	**259.6**	**10**	**162**	**421.6**		
20 Jan							
Leg A	14	30.8	0	0	30.8	0.15	2
Leg B	17	37.4	1	16.2	53.6	0.04	11
Leg C	23	50.6	1	16.2	66.8	0.11	59
Leg D	14	30.8	2	32.4	63.2	0.18	82
Leg E	16	35.2	3	48.6	83.8	0.28	48
Leg F	17	37.4	0	0	37.4	N/A	0
Leg G	18	39.6	0	0	39.6	N/A	0
Leg H	17	37.4	2	32.4	69.8	0.3	55
Total	**136**	**299.2**	**9**	**145.8**	**445**		
31 Jan							
Leg A	21	46.2	3	48.6	94.8	0.24	99
Leg B	16	35.2	3	48.6	83.8	0.23	94
Total A-B	**37**	**81.4**	**6**	**97.2**	**178.6**		

Table 2: Scan strategy for Packer John and Snowbank radars for the cases discussed here including 360° azimuthal or Plain Position Indicator (PPI) scans and vertical cross sections or Range Height Indicator (RHI) scans upwind and downwind from the radar. The RHI scans along the UWKA flight track and PPI scans used for this analysis are highlighted in bold. Both radars conducted Z_{dr} calibration scans at 89° elevation angle every 12 minutes.

	Snowbank	**Packer John**
19 Jan	**PPIs @ -1° to 70° elev every 6 min**	PPIs @ -1° elev every 5 min RHIs @ 35°/215° azim, 37°/217°, **39°/219°**, 41°/221°, 42°/222°, 43°/223°
20 Jan	Not operational	**PPIs @ -1° to 3° elev every 1° and 1 min** No RHIs
31 Jan	**PPIs @ -1° to 70° elev every 6 min**	PPIs @ -1° to 17° elev every 1° and 1 min RHIs @ 86°/266° azim, 88°/268°, **90°/270°**, 92°/272°, 93°/273°, 94°/274°

Table 3: Summary of measurements during the three events discussed here.

	19-Jan (Leg A-B)	**20-Jan**	**31-Jan**
Surface snowfall (Friedrich et al. 2020)			
Total amount of snowfall (m^3)	123,220	241,260	339,540
Snowfall range (mm)	0.05-0.14	0.05-1.5	0.05-0.25
Start of precipitation after seeding (min)	45	40	12
Area covered (km^2)	2,327	1,838	2,410
Seeding operations			
Successful seeding legs (total duration)	2 (26 min)	8 (82 min)	2 (19 min)
total AgI from BIP	32.4	145.8	81.4
total AgI from EJ	55	299.2	97.2
total AgI	87.4	445	178.6
Environmental conditions (outside of the seeding lines)			
Seeding Aircraft			
Mean LWC ($g\ m^{-3}$)	0.11-0.17	0.04-0.3	0.23-0.24

Wind speed (m s^{-1})	15-18	10	30-40
T (°C)	-16 to -14	-15 to -14	-13
UWKA			
Mean LWC (g m^{-3})	0.1-0.2	0.1-0.2	N/A
Max LWC along a leg (g m^{-3})	0.3-0.4	0.45-0.6	0.4
Cloud droplet concentration (cm^{-3}) D < 50 um	< 30	< 30	20-30
Diameter of cloud droplets (μm)	20 to 30	20 to 30	N/A
Mean ice particle concentration (L^{-1}) D > 100 μm	< 0.1	< 0.1	N/A
Max ice particle concentration along a leg (L^{-1})	1 - 2 only over the highest terrain	1 - 5 only over the highest terrain	N/A
Range cloud top height (km)	3-4.5	3.5-4	4.8-5.2
Presence of supercooled drizzle drops	Isolated pockets 50 < D < 100 μm drops	Extensive regions 50 < D < 150 μm drops	Widespread 50 < D < 200 μm drops
Sounding			
T (°C) @ cloud top height	- 13 to -15	- 13 to -17	-13-15

q (g kg^{-1}) @ cloud top height	1.5-1.8	1-1.5	1.6-2
Shear (s^{-1}) @ cloud top height	> 0.02	> 0.03	> 0.03
Ice initiation (values within the seeding lines)			
Approx. time between seeding and first plumes (Z_e > 5 dBZ$_e$) in minutes	20 - 30	15 - 30	
LWC (g m^{-3})	< 0.01 - 0.05	< 0.01 - 0.143	N/A
IWC (g m^{-3})	0.10 - 0.48	0.10 - 0.27	N/A
Concentration of ice particles (L^{-1}) D > 100 µm	2.5 - 8.0 (mean) 21 (max)	1.0 to 3.8 (mean) 26 (max)	N/A
Ice Particle Habits	rimed ice; dendritic crystals; irregular shaped ice	heavily rimed ice, irregular shaped ice	N/A
Snow Growth			
Dendritic growth	Observed 36-78 min after seeding (Lines A'-B')	Observed 60-150 min after seeding (primarily Lines C'-H')	Observed 40-55 min after seeding (Lines A'-B')
Z_e gradient below the DGL (dBZ$_e$ km^{-1})	3	4.6	6.25

Figure Caption List

Figure 1: Schematic of cloud seeding operations and related research questions.

Figure 2: Topographic map showing the flight tracks for the seeding aircraft (solid lines) and the UWKA aircraft (dashed lines) on 19 Jan (red lines), 20 Jan (blue lines), and 30 Jan 2017 (green line). Range of cruising altitudes (in MSL) is indicated for each aircraft and day; leg notation is indicated for 19 Jan; winds at the cruising altitude of the seeding aircraft are indicated (half barb: 2.5 m s^{-1} and full barb: 5 m s^{-1}). Locations of the ground-based radar at Packer John and Snowbank and the sounding at Crouch are shown as diamond and circle symbols, respectively. Distance from the Packer John radar along the UWKA track is indicated. The 50-km radius around each radar is highlighted as a gray area. Mountain ranges discussed in the text are highlighted.

Figure 3: Vertical profile of a) temperature, b) equivalent potential temperature, and c) wind speed, and d) direction from the sounding at Crouch closest to the seeding line observations at 1600 UTC on 19 Jan (red lines), 0000 UTC on 20 Jan (blue lines), and 1600 UTC on 31 Jan (green lines). Gray, dashed line represents the height of PJ. Range of cloud top heights as the seeding lines pass through the ROD are indicated by unfilled boxes in a); range of UWKA flights is indicated by filled boxes (color-coded by day) associated with the cloud top range.

Figure 4: Location of flares (upper panel), 10-min averaged liquid water content (lower panel) measured by the seeding aircraft for each seeding flight leg on a) 19 Jan, b) 20 Jan, and c) 31 Jan. Upper panels: The direction of the flight leg is indicated by gray arrows in the upper panel.

Circles (lines) indicate the location of the ejectable (burn-in-place) flares. Lower panels: Data were averaged over 10 min. Numbers in brackets indicate the mean temperature during the seeding flight leg.

Fig. 5: Combined maximum Z_e between the surface and 1 km AGL from the PJ and SB DOW radars on 19 Jan at a) 1710, b) 1719, c) 1729, and d) 1746 UTC. Radar locations are indicated by the star symbols and maximum range of 50 km with a circle centered around each radar. UWKA Legs 6-8 are highlighted as a red dashed line; position of the UWKA aircraft at the radar times is highlighted by an aircraft symbol. Seeding aircraft legs are indicated as black dashed. Seeding Lines A’ and B’ associated with Legs A and B are highlighted.

Fig. 6: Evolution of Z_e from the WCR during UWKA Legs 4-10 on 19 Jan. Times given indicate the beginning and end of each leg, arrows indicate flight direction for that leg. In all cases, wind is from left to right. A clear signal from seeding line A is detected in all seven legs. Seeding Line B is detectable in the last five legs. Thick, solid lines contour regions of enhanced reflectivity due to seeding. Dashed lines show similar regions of increased reflectivity from seeding that are interspersed with areas of natural reflectivity enhancement. The white belt is the WCR blind zone centered at flight level.

Fig. 7: a) Hydrometeor size distributions measured by the *in-situ* probes on the UWKA in Line A’ during UWKA Legs 4-10 on 19 Jan sampled between 1640-1816 UTC. b) Particle images from the 2DS from seeding line passage are shown. The frame size is 1.6 mm from top to bottom as indicated in the top frame, the labels on the right indicate the UWKA leg number and the

duration between the release of the seeding material and sampling by the UWKA. c) Vertical profiles of Ze from the WCR in seeding Line A for each of the UWKA legs shown in Fig. 5. Each box is 8 km wide and 4 km tall (leg number and time on the bottom, same as in b). The gray bar indicates that portion of the UWKA track that was in the seeding line for each of the seven passes, and used for the size distribution in panel (a). Maximum *LWC* observed at flight level within the seeded line is indicated on the top.

Fig. 8: As in Fig. 7 except for Line B' on 19 Jan.

Fig. 9: RHI composite between 1654-1742 UTC along the flight track at 39° azimuthal direction on 19 Jan showing dual-polarization variables for a) Line A' and b) Line B' with K_{dp} on the top, Z_{dr} in the middle, and Z_e in the lower panel. Terrain (cone of silence and area below the lowest radar beam) is indicated in dark (light) gray shading. PJ is shown as a star symbol and North Folk Range is highlighted. Temperatures were derived from the nearest sounding at 1600 UTC at Crouch (location shown in Fig. 2). Radar times are indicated in the top panel; minutes after seeding in the middle panel. Red shading indicates the altitude range of the UWKA flight tracks.

Fig. 10: Similar to Fig. 6 except for the evolution of near-vertical Doppler radial velocity from the WCR during UWKA Legs 6-8 on 19 Jan. Blue indicates upward motion and red indicates downward motion. Note, that the color scale has been shifted by 1 m s^{-1} to account for an *expected* nominal terminal fall velocity of the main scatterers. In this context blue (red) regions indicate areas of upward (downward) moving *air*. Black lines contour regions of enhanced reflectivity due to seeding.

Fig. 11: a) PPI of Z_e at 2.8 km MSL on 19 Jan. Each panel is 50 km x 100 km. Mean dual-polarization variables are analyzed for Line A' indicated within the black box. Color bars for Ze and terrain are shown in Fig. 4. b-e) Vertical profiles of mean b) Z_e, c) Z_{dr}, d) K_{dp}, and e) ρ_{hv} as a function of time (color coded). Horizontal lines indicate -10 and -15 °C temperatures from the 1600 UTC sounding at Crouch. Red shading indicates the altitude range of the UWKA flight tracks.

Fig. 12: As Fig. 5, but Z_e from Packer John radar for 20 Jan at a) 0047, b) 0116, c) 0143, and d) 0211 UTC.

Fig. 13: As in Fig. 6, except for showing UWKA Legs 7-10 on 20 Jan. Since the UWKA passed through the NW end of the seeding lines, pairs of lines show up as a single intersect and are therefore labeled as pairs.

Fig. 14: Vertical profile of Z_e (color-coded) and Doppler velocity (black lines in m s^{-1}) observed by the MRR at Packer John on 20 Jan between 0045-0200 UTC. Seeding Lines C'-H' are labeled. Blue shading indicates the altitude range of the UWKA flight tracks.

Fig. 15: a-c) Hydrometeor size distributions measured by *in-situ* probes on the UWKA in a) Lines C'-D', b) Lines E'-F', and d) Lines G'-H' corresponding to UWKA Legs 7-10 on 20 Jan (cp. Fig. 7). d-e) Vertical profiles of Ze from the WCR for d) Lines C'-D', e) Lines E'-F', and f) Lines G'-H' shown in a-c). Each box is 9 km wide and 5 km tall. The gray bar indicates that portion of the UWKA leg from which the size distributions were constructed. The labels below

each image indicate the UWKA leg number and the duration of the gray bar. Labels above indicate the maximum LWC observed within the gray bar.

Figure 16: As Fig. 11, but a) PPI of Z_e at 2.8 km MSL for four radar times on 20 Jan. ROD is divided into four 8 km x 60 km boxes (Boxes 1-4) indicating the analysis area. Each panel is 50 km x 60 km. b-e) Vertical profiles of b) area with Z_e > 15 dBZ, c) $\overline{Z_e}$, d) $\overline{K_{dp}}$, and e) $\overline{Z_{dr}}$ as a function of time (color coded). Horizontal lines indicate -5, -10, -15 °C temperatures from the 0000 UTC sounding at Crouch. Gray shading indicates height levels that might be partially affected by radar beam blockage. Blue shading indicates the altitude range of the UWKA flight tracks.

Fig. 17: As Fig. 11, but for Z_e observed by the SB DOW radar on 31 Jan at a) 2110, b) 2122, c) 2134, and d) 2146 UTC.

Fig. 18: a) Vertical west-east cross section of Z_e from the UWKA flight Legs 6-9. Times and flight direction are indicated. Terrain is shown in black. b) West-east RHI scan along flight track on 31 Jan observed by the Packer John DOW radar at 2114 UTC, 2124 UTC, 2130 UTC, and 2142 UTC. UWKA flight Legs 6-9 and the position of the aircraft are indicated as a red line and red aircraft symbol. Lines A' and B' indicating the BIP flares and Lines A'' and B'' the EJ flares. Dark gray shading indicates topography; lighter gray shading indicates approximated radar coverage.

Figure 19: As Fig. 11, but showing a) PPI of Ze at 2.8 km at six radar times on 31 Jan. Each panel is 50 x 95 km. b-e) Vertical profiles of mean Z_e, Z_{dr}, K_{dp}, and ρ_{hv} over all seeding lines. Horizontal lines indicate -10, -15°C temperatures from the closest sounding at 1600 UTC sounding at Crouch. Green shading indicates the altitude range of the UWKA flight tracks.

Fig. 20: A conceptual illustration of the seeding lines and snowfall with a) weak horizontal winds (19 and 20 Jan) and b) strong horizontal winds on 31 Jan (modified Fig. 1 in French et al. 2018). Top panels show temporal evolution of the seeding lines with yellow–orange–red colors indicating locations and relative magnitude of Z_e as a vertical cross section along the UWKA flight track. Bottom panels show a plain view of the distribution of total accumulated liquid equivalent snowfall with intensities increasing from yellow to orange to red colors (modified from Friedrich et al. 2020). Observations are limited to the maximum radar range; accumulations most likely occurred farther downwind and beyond the radar range. Yellow dots show locations of ground-based radars, the solid (dash) line represents a typical flight track for the seeding (Wyoming King Air) aircraft.

1213 **Figures**

1214 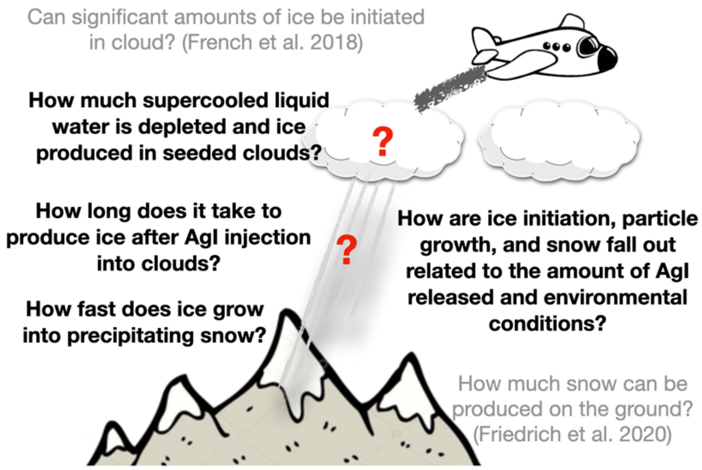

1215 Figure 1: Schematic of cloud seeding operations and related research questions.

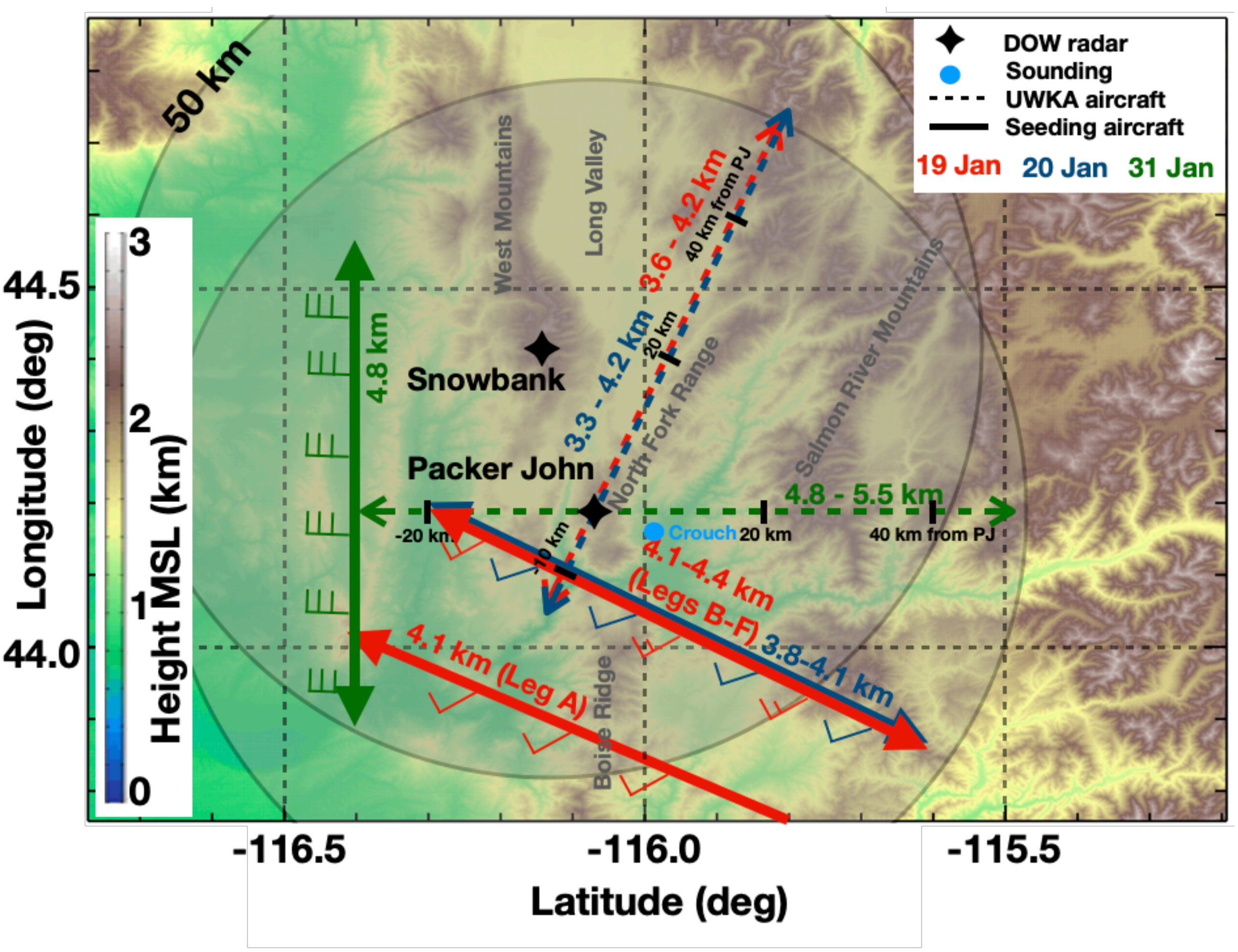

Figure 2: Topographic map showing the flight tracks for the seeding aircraft (solid lines) and the UWKA aircraft (dashed lines) on 19 Jan (red lines), 20 Jan (blue lines), and 30 Jan 2017 (green line). Range of cruising altitudes (in MSL) is indicated for each aircraft and day; leg notation is indicated for 19 Jan; winds at the cruising altitude of the seeding aircraft are indicated (half barb: 2.5 m s^{-1} and full barb: 5 m s^{-1}). Locations of the ground-based radar at Packer John and Snowbank and the sounding at Crouch are shown as diamond and circle symbols, respectively. Distance from the Packer John radar along the UWKA track is indicated. The 50-km radius around each radar is highlighted as a gray area. Mountain ranges discussed in the text are highlighted.

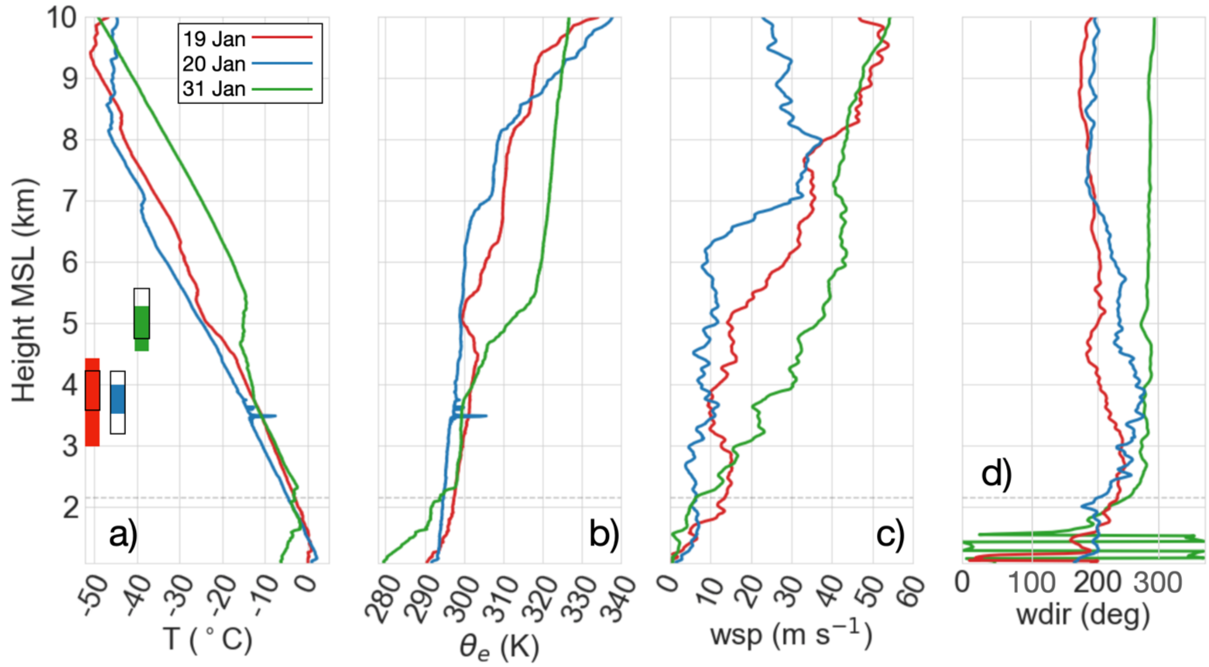

Figure 3: Vertical profile of a) temperature, b) equivalent potential temperature, and c) wind speed, and d) direction from the sounding at Crouch closest to the seeding line observations at 1600 UTC on 19 Jan (red lines), 0000 UTC on 20 Jan (blue lines), and 1600 UTC on 31 Jan (green lines). Gray, dashed line represents the height of PJ. Range of cloud top heights as the seeding lines pass through the ROD are indicated by unfilled boxes in a); range of UWKA flights is indicated by filled boxes (color-coded by day) associated with the cloud top range.

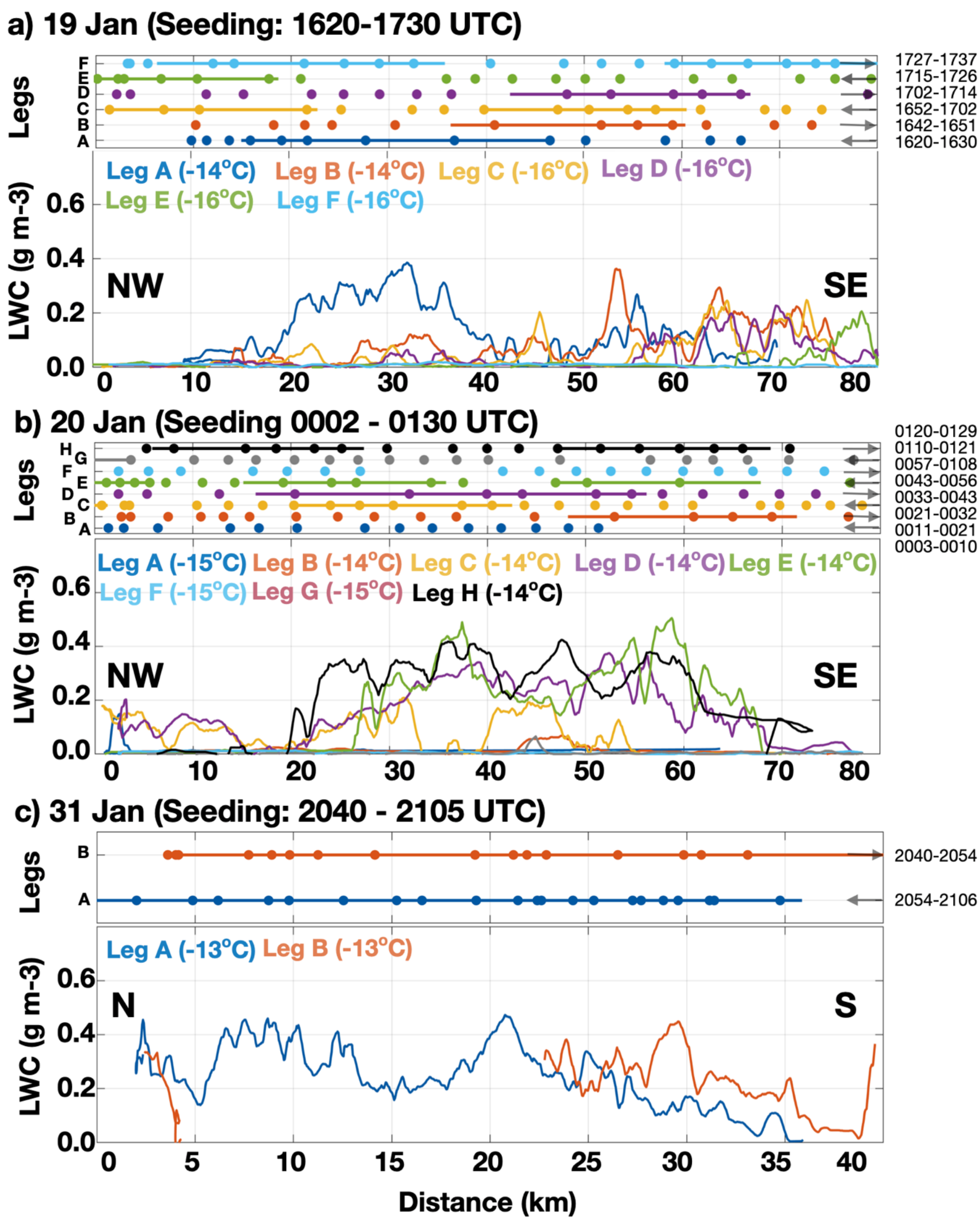

Figure 4: Location of flares (upper panel), 10-min averaged liquid water content (lower panel) measured by the seeding aircraft for each seeding flight leg on a) 19 Jan, b) 20 Jan, and c) 31

Jan. Upper panels: The direction of the flight leg is indicated by gray arrows in the upper panel. Circles (lines) indicate the location of the ejectable (burn-in-place) flares. Lower panels: Data were averaged over 10 min. Numbers in brackets indicate the mean temperature during the seeding flight leg.

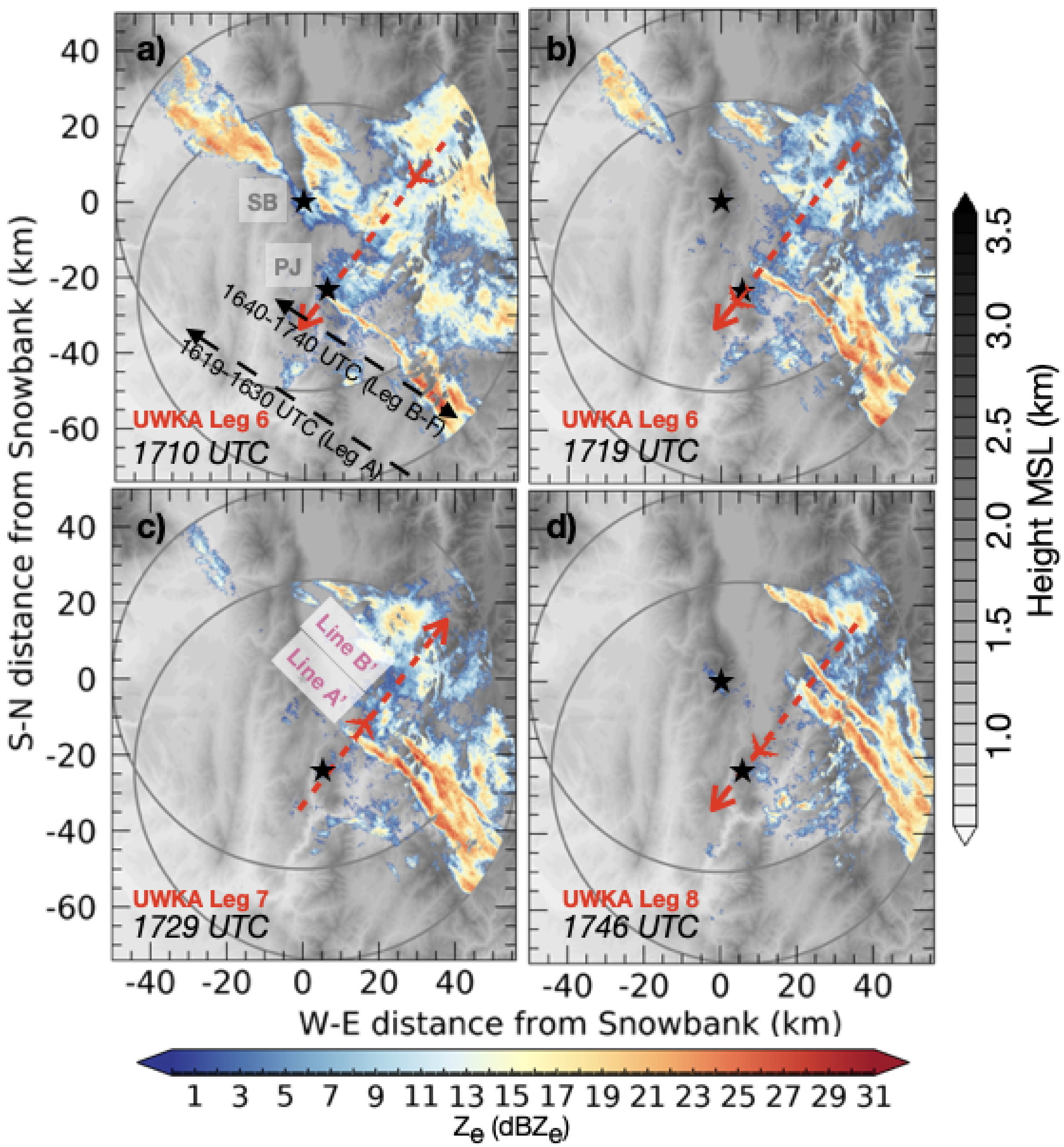

Fig. 5: Combined maximum Z_e between the surface and 1 km AGL from the PJ and SB DOW radars on 19 Jan at a) 1710, b) 1719, c) 1729, and d) 1746 UTC. Radar locations are indicated by the star symbols and maximum range of 50 km with a circle centered around each radar. UWKA Legs 6-8 are highlighted as a red dashed line; position of the UWKA aircraft at the radar times is highlighted by an aircraft symbol. Seeding aircraft legs are indicated as black dashed. Seeding Lines A' and B' associated with Legs A and B are highlighted.

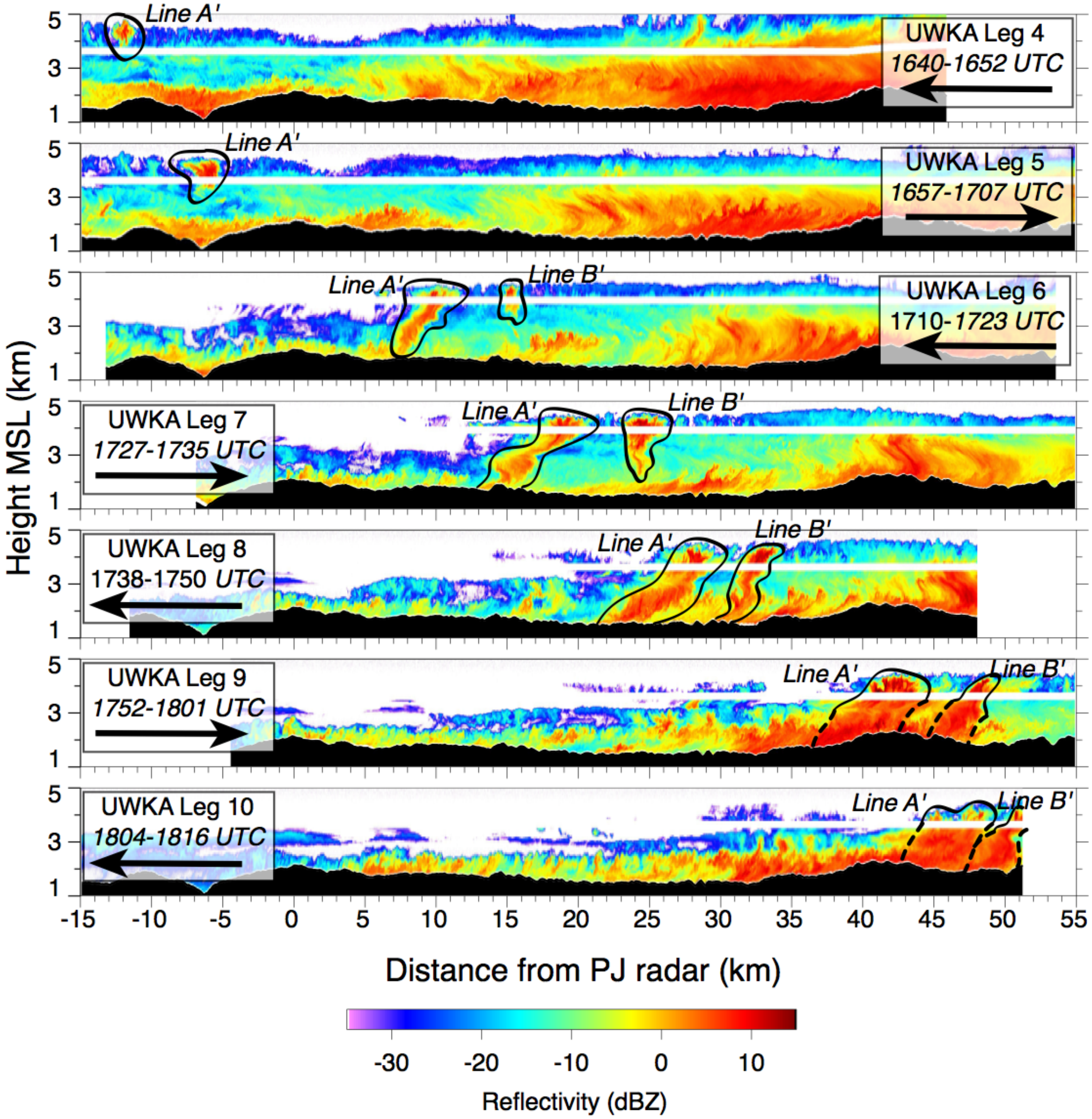

Fig. 6: Evolution of Z_e from the WCR during UWKA Legs 4-10 on 19 Jan. Times given indicate the beginning and end of each leg, arrows indicate flight direction for that leg. In all cases, wind is from left to right. A clear signal from seeding line A is detected in all seven legs. Seeding Line B is detectable in the last five legs. Thick, solid lines contour regions of enhanced reflectivity due to seeding. Dashed lines show similar regions of increased reflectivity from seeding that are

interspersed with areas of natural reflectivity enhancement. The white belt is the WCR blind zone centered at flight level.

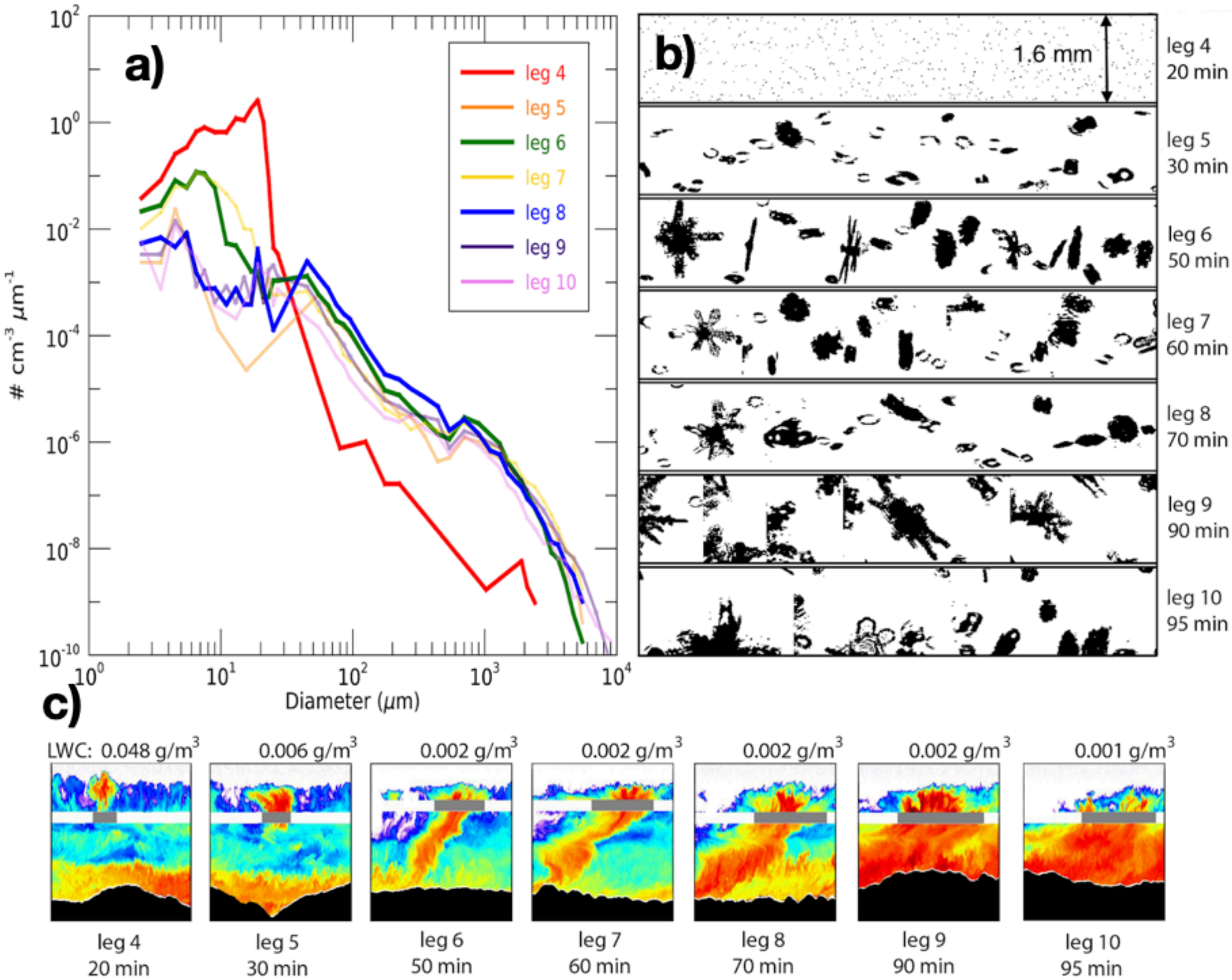

Fig. 7: a) Hydrometeor size distributions measured by the *in-situ* probes on the UWKA in Line A' during UWKA Legs 4-10 on 19 Jan sampled between 1640-1816 UTC. b) Particle images from the 2DS from seeding line passage are shown. The frame size is 1.6 mm from top to bottom as indicated in the top frame, the labels on the right indicate the UWKA leg number and the duration between the release of the seeding material and sampling by the UWKA. c) Vertical profiles of Ze from the WCR in seeding Line A for each of the UWKA legs shown in Fig. 5. Each box is 8 km wide and 4 km tall (leg number and time on the bottom, same as in b). The gray bar indicates that portion of the UWKA track that was in the seeding line for each of the

seven passes, and used for the size distribution in panel (a). Maximum *LWC* observed at flight level within the seeded line is indicated on the top.

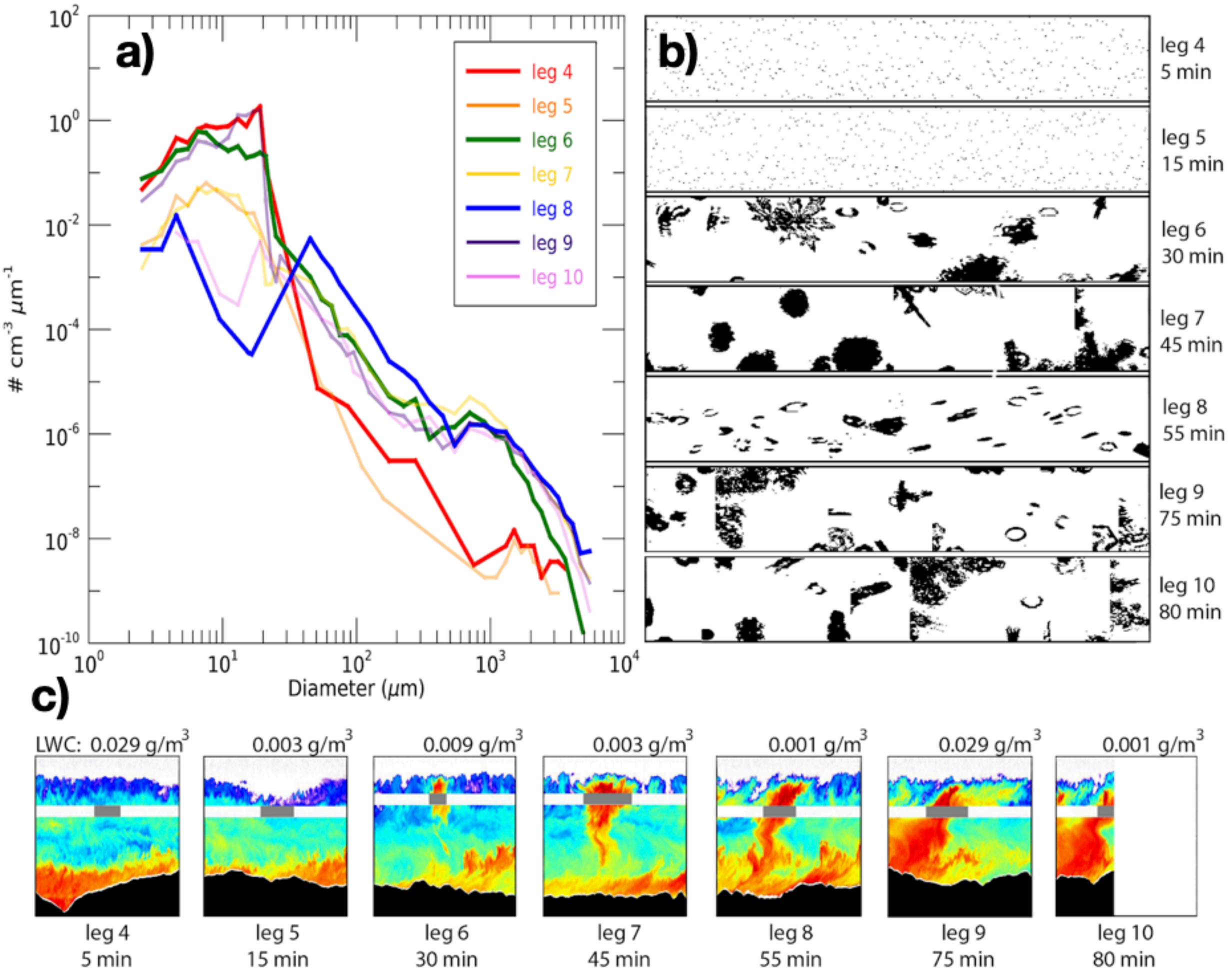

Fig. 8: As in Fig. 7 except for Line B’ on 19 Jan.

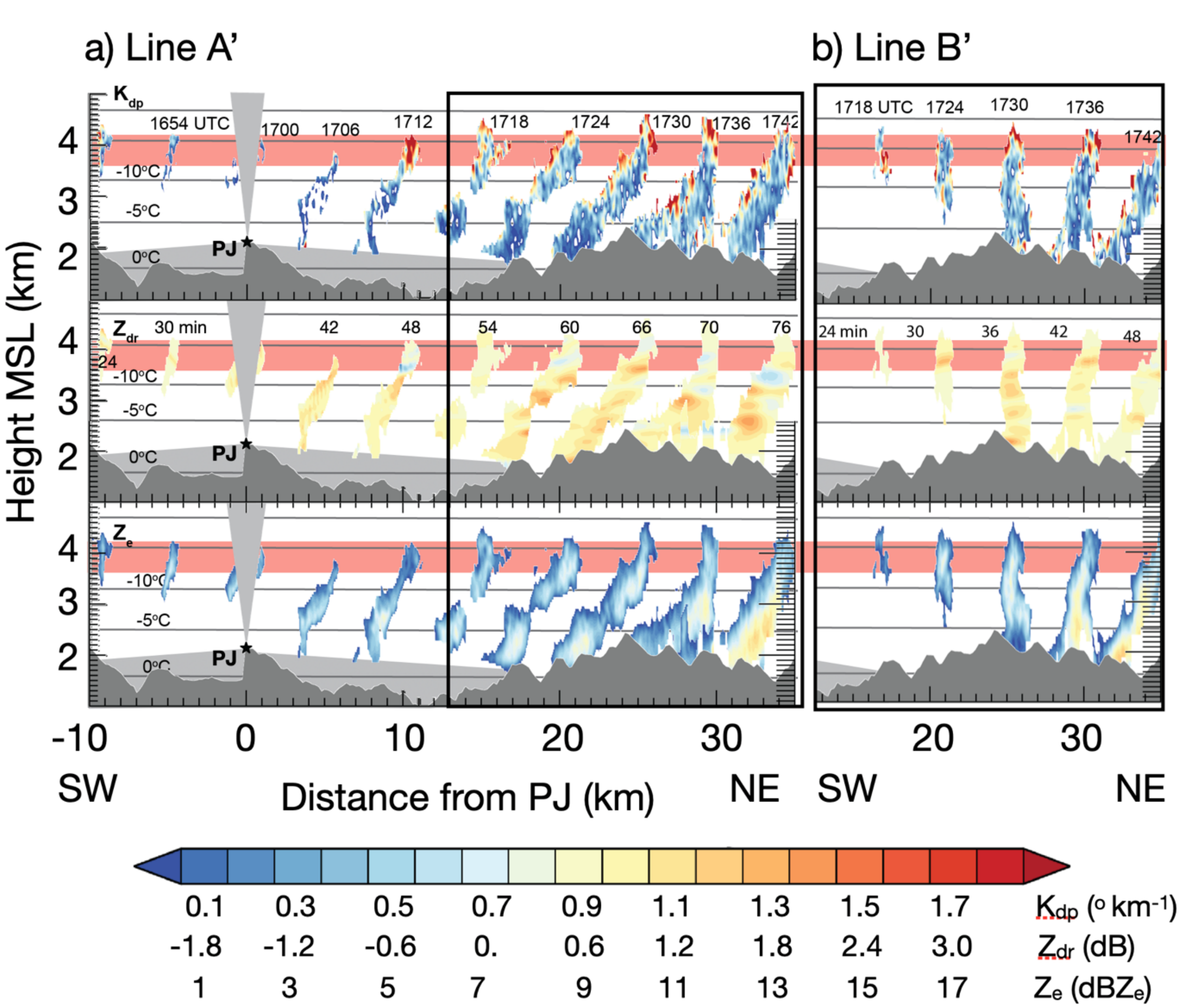

Fig. 9: RHI composite between 1654-1742 UTC along the flight track at 39° azimuthal direction on 19 Jan showing dual-polarization variables for a) Line A' and b) Line B' with K_{dp} on the top, Z_{dr} in the middle, and Z_e in the lower panel. Terrain (cone of silence and area below the lowest radar beam) is indicated in dark (light) gray shading. PJ is shown as a star symbol and North Folk Range is highlighted. Temperatures were derived from the nearest sounding at 1600 UTC at Crouch (location shown in Fig. 2). Radar times are indicated in the top panel; minutes after seeding in the middle panel. Red shading indicates the altitude range of the UWKA flight tracks.

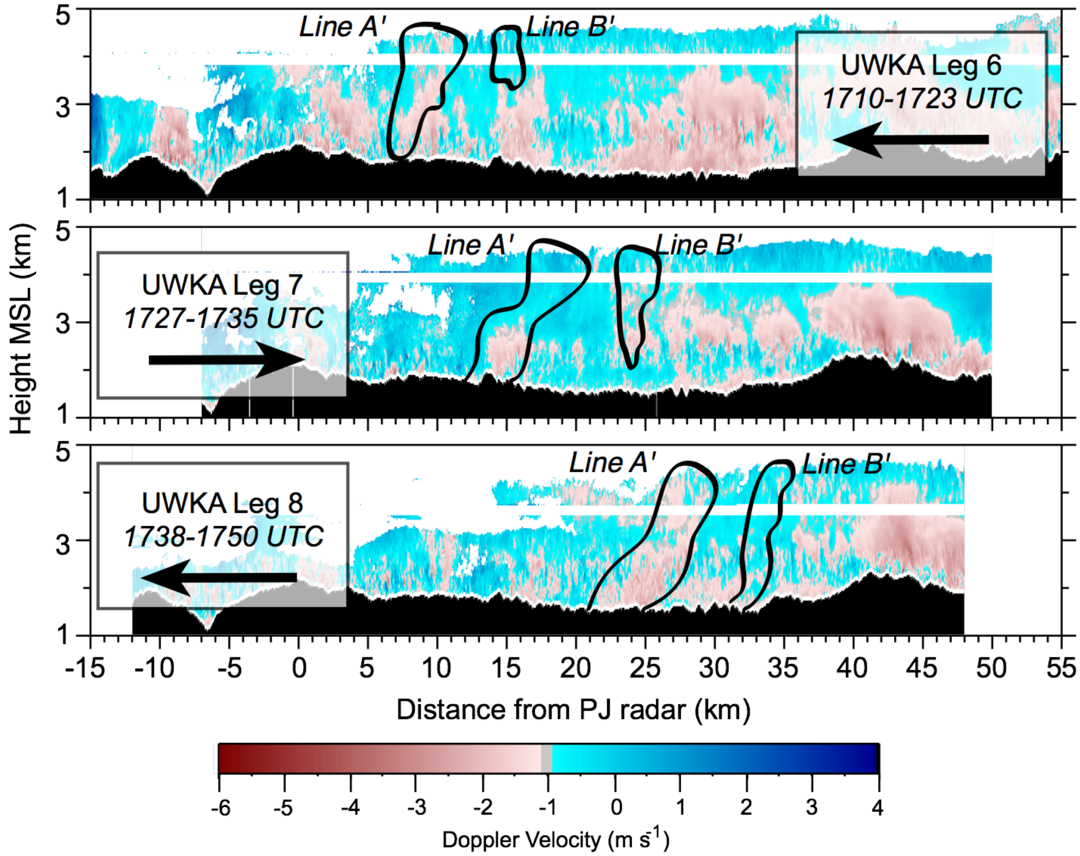

Fig. 10: Similar to Fig. 6 except for the evolution of near-vertical Doppler radial velocity from the WCR during UWKA Legs 6-8 on 19 Jan. Blue indicates upward motion and red indicates downward motion. Note, that the color scale has been shifted by 1 m s^{-1} to account for an *expected* nominal terminal fall velocity of the main scatterers. In this context blue (red) regions indicate areas of upward (downward) moving *air.* Black lines contour regions of enhanced reflectivity due to seeding.

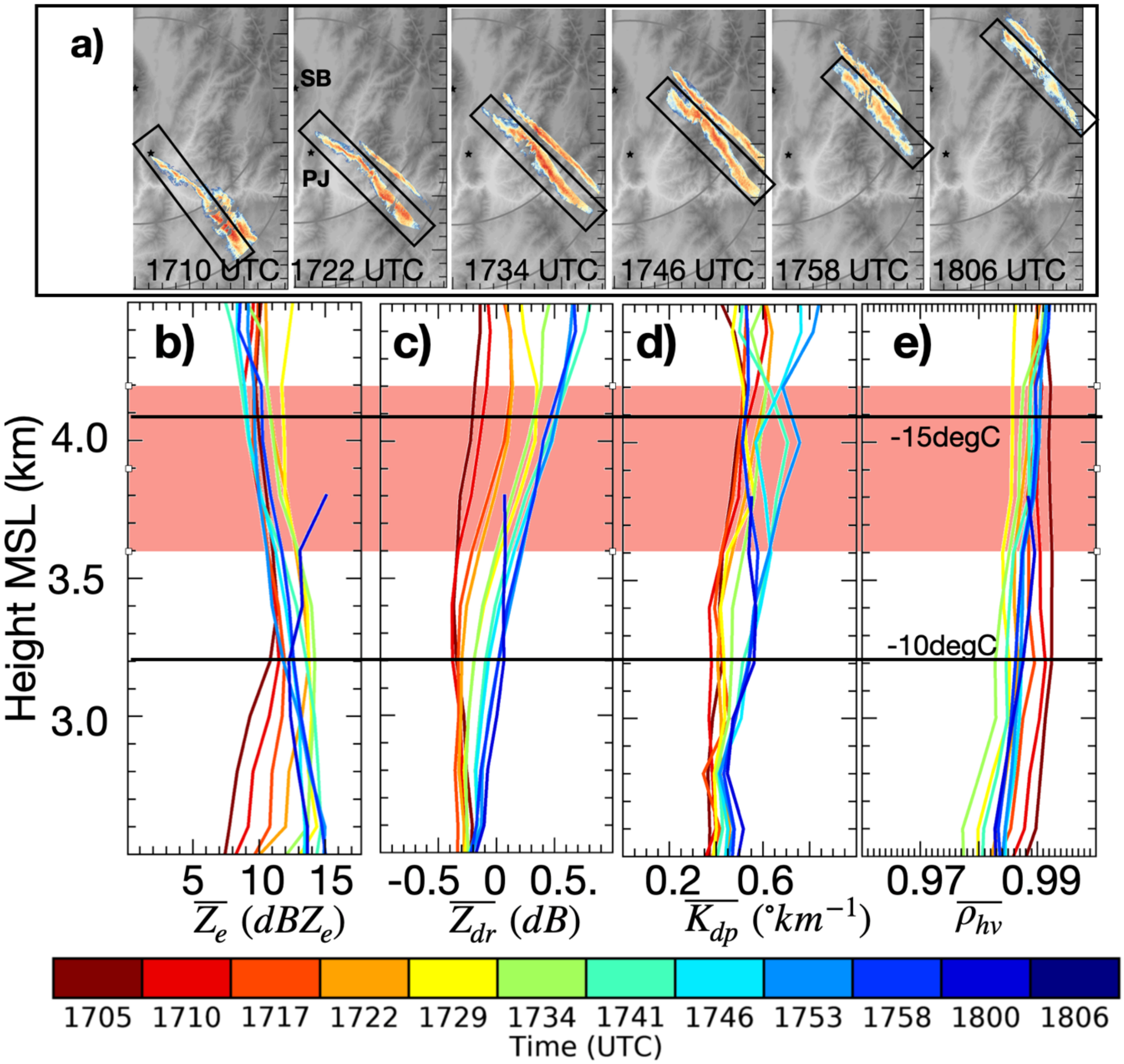

Fig. 11: a) PPI of Z_e at 2.8 km MSL on 19 Jan. Each panel is 50 km x 100 km. Mean dual-polarization variables are analyzed for Line A' indicated within the black box. Color bars for Ze and terrain are shown in Fig. 4. b-e) Vertical profiles of mean b) Z_e, c) Z_{dr}, d) K_{dp}, and e) ρ_{hv} as a function of time (color coded). Horizontal lines indicate -10 and -15 °C temperatures from the 1600 UTC sounding at Crouch. Red shading indicates the altitude range of the UWKA flight tracks.

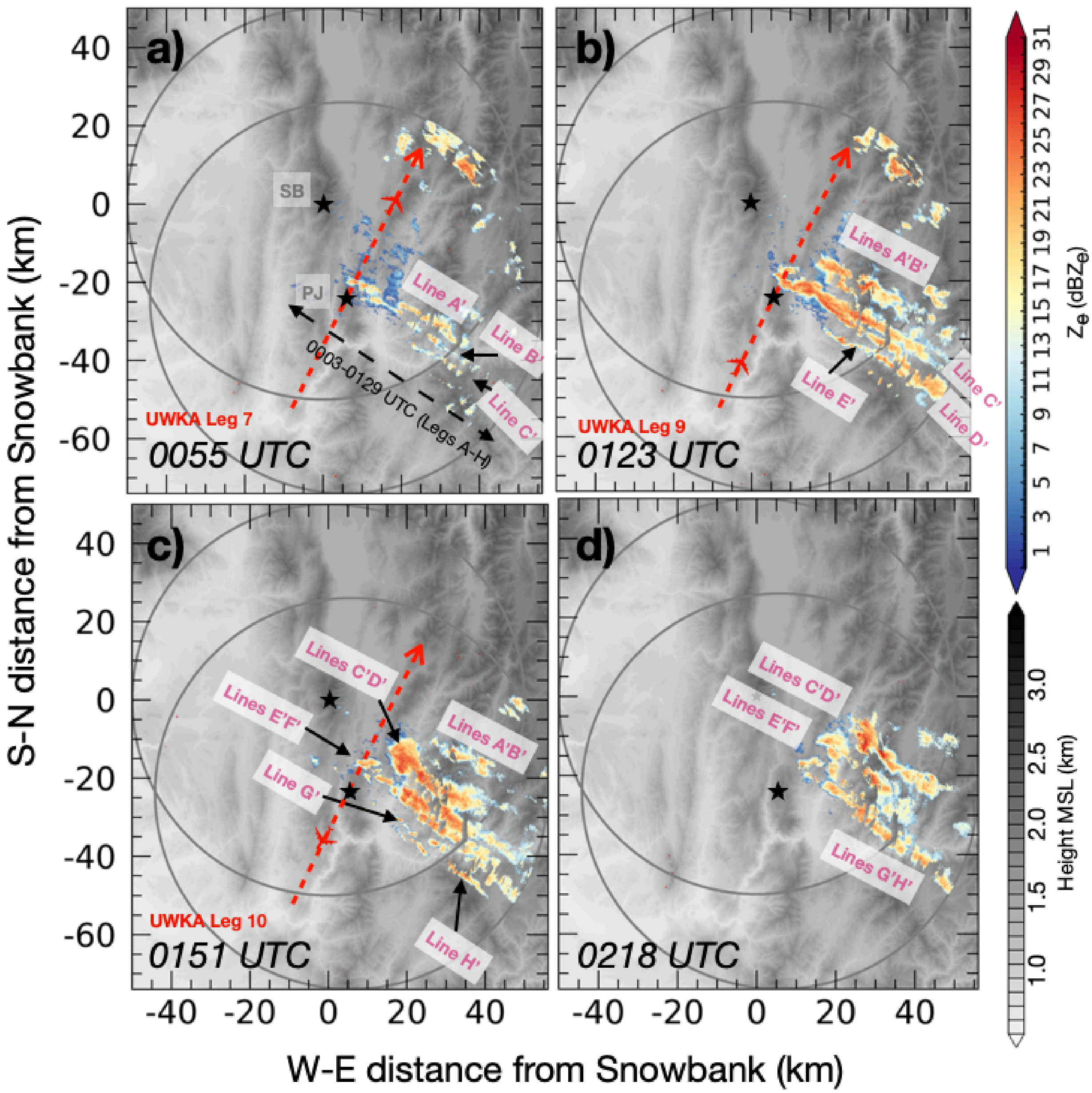

Fig. 12: As Fig. 5, but Z_e from Packer John radar for 20 Jan at a) 0047, b) 0116, c) 0143, and d) 0211 UTC.

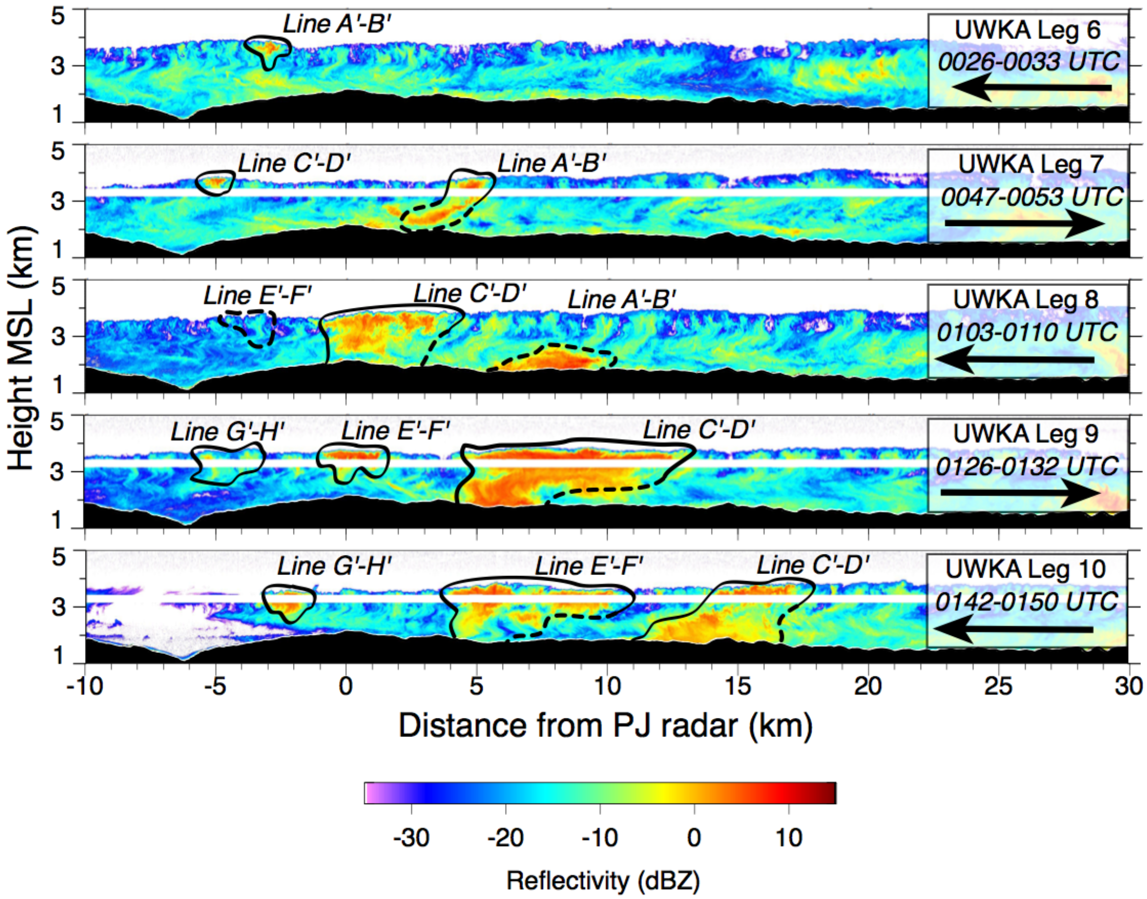

Fig. 13: As in Fig. 6, except for showing UWKA Legs 7-10 on 20 Jan. Since the UWKA passed through the NW end of the seeding lines, pairs of lines show up as a single intersect and are therefore labeled as pairs.

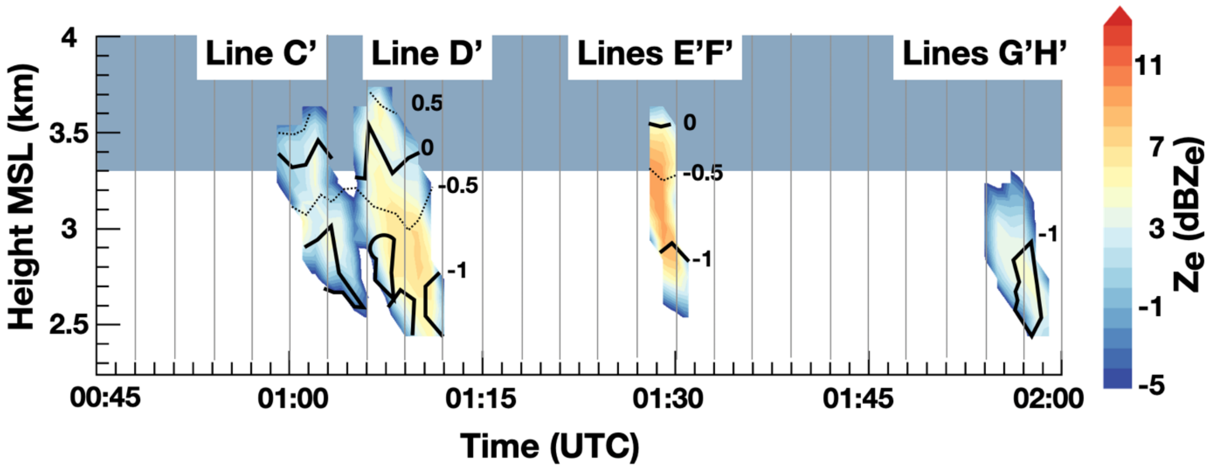

Fig. 14: Vertical profile of Z_e (color-coded) and Doppler velocity (black lines in m s^{-1}) observed by the MRR at Packer John on 20 Jan between 0045-0200 UTC. Seeding Lines C'-H' are labeled. Blue shading indicates the altitude range of the UWKA flight tracks.

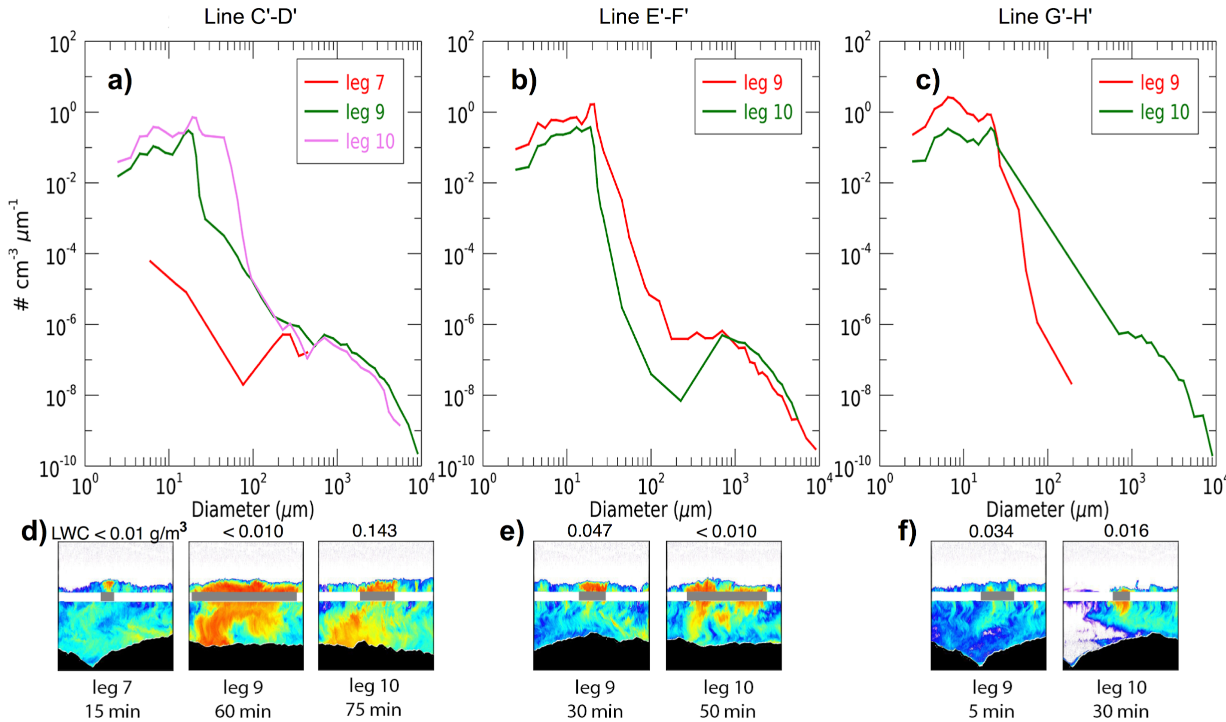

Fig. 15: a-c) Hydrometeor size distributions measured by *in-situ* probes on the UWKA in a) Lines C'-D', b) Lines E'-F', and d) Lines G'-H' corresponding to UWKA Legs 7-10 on 20 Jan (cp. Fig. 7). d-e) Vertical profiles of Ze from the WCR for d) Lines C'-D', e) Lines E'-F', and f) Lines G'-H' shown in a-c). Each box is 9 km wide and 5 km tall. The gray bar indicates that portion of the UWKA leg from which the size distributions were constructed. The labels below each image indicate the UWKA leg number and the duration of the gray bar. Labels above indicate the maximum *LWC* observed within the gray bar.

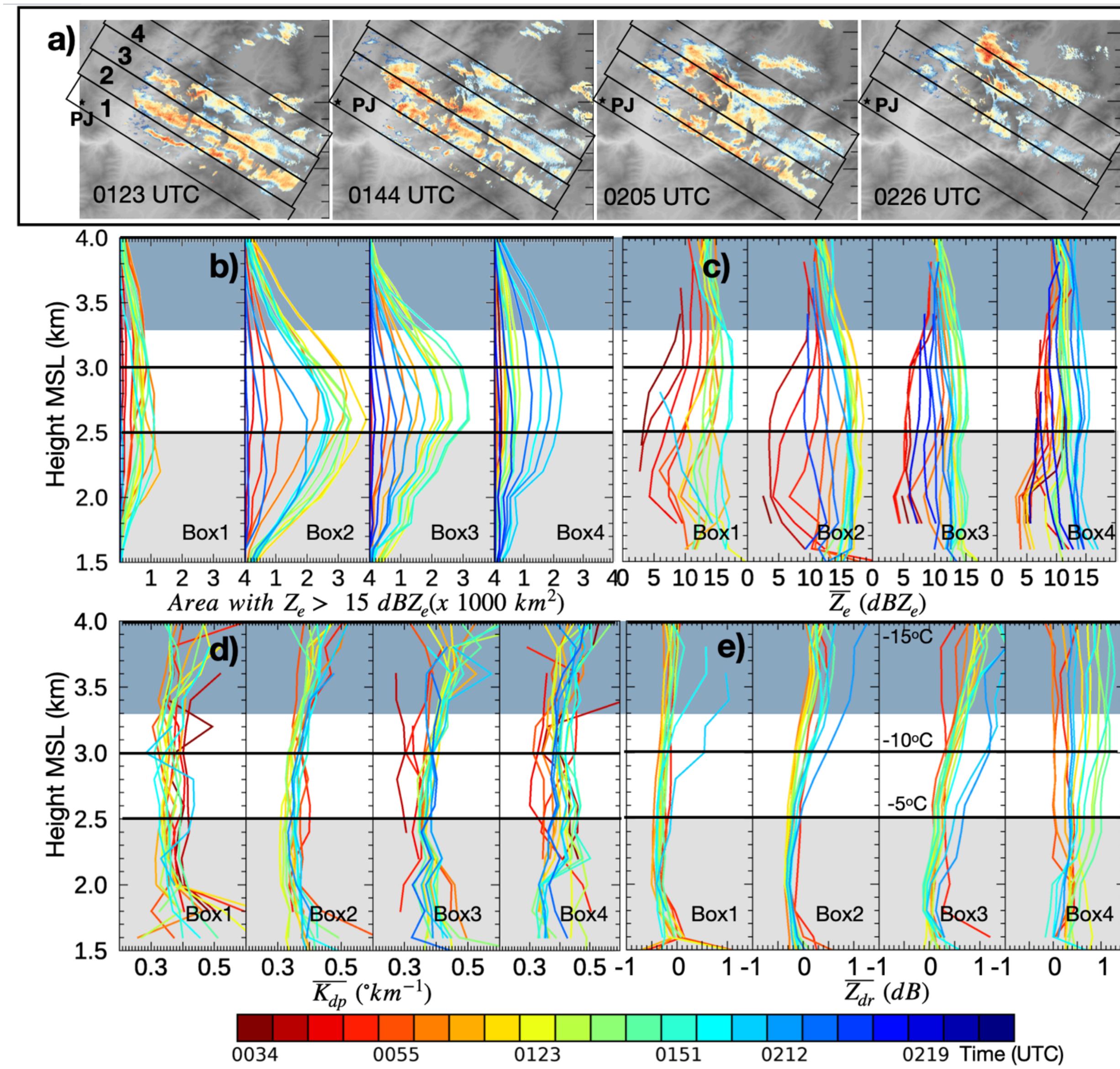

Figure 16: As Fig. 11, but a) PPI of Z_e at 2.8 km MSL for four radar times on 20 Jan. ROD is divided into four 8 km x 60 km boxes (Boxes 1-4) indicating the analysis area. Each panel is 50 km x 60 km. b-e) Vertical profiles of b) area with Z_e > 15 dBZ, c) $\overline{Z_e}$, d) $\overline{K_{dp}}$, and e) $\overline{Z_{dr}}$ as a function of time (color coded). Horizontal lines indicate -5, -10, -15 °C temperatures from the 0000 UTC sounding at Crouch. Gray shading indicates height levels that might be partially affected by radar beam blockage. Blue shading indicates the altitude range of the UWKA flight tracks.

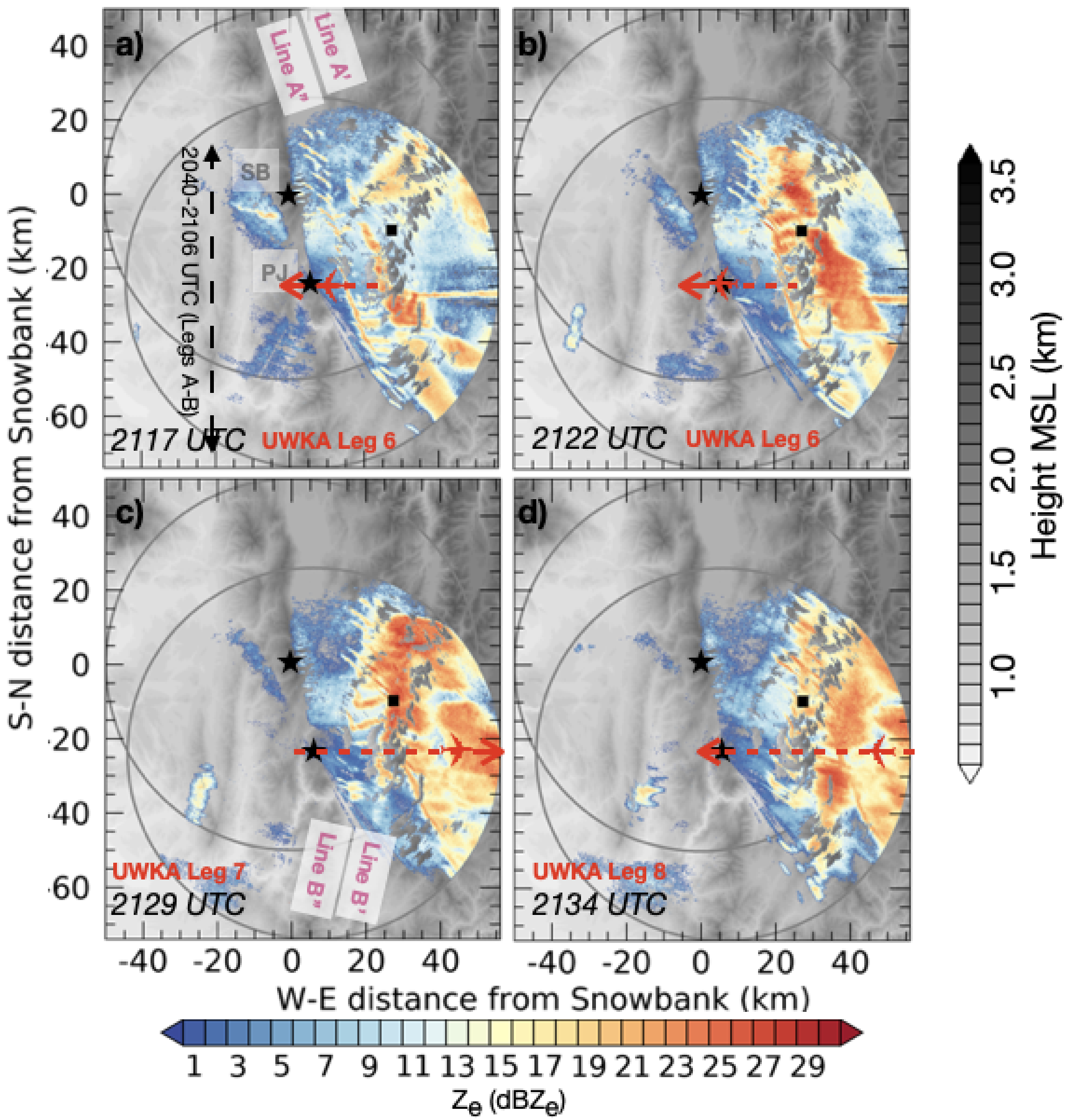

Fig. 17: As Fig. 11, but for Z_e observed by the SB DOW radar on 31 Jan at a) 2110, b) 2122, c) 2134, and d) 2146 UTC.

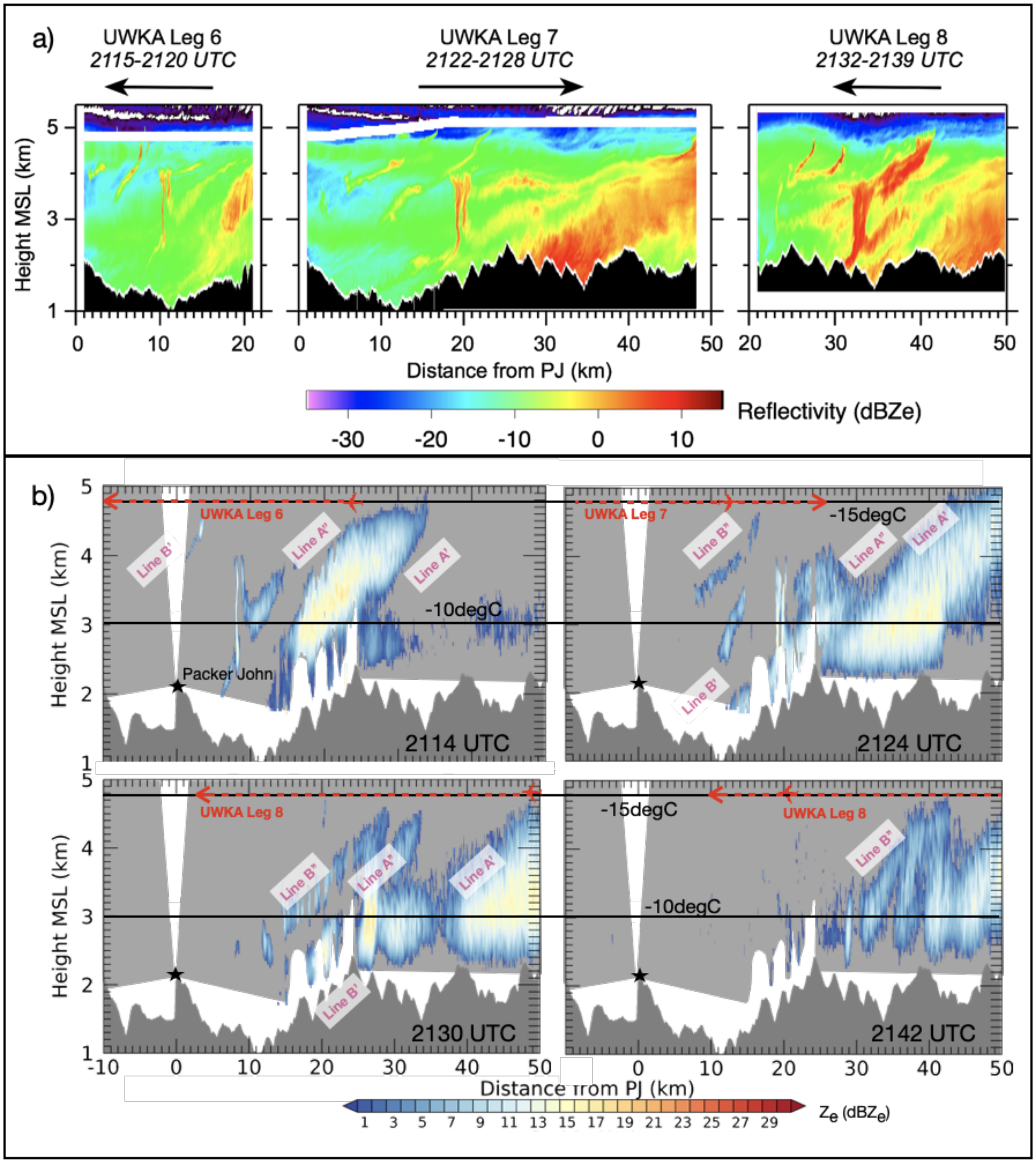

Fig. 18: a) Vertical west-east cross section of Z_e from the UWKA flight Legs 6-9. Times and flight direction are indicated. Terrain is shown in black. b) West-east RHI scan along flight track on 31 Jan observed by the Packer John DOW radar at 2114 UTC, 2124 UTC, 2130 UTC, and 2142 UTC. UWKA flight Legs 6-9 and the position of the aircraft are indicated as a red line and red aircraft symbol. Lines A' and B' indicating the BIP flares and Lines A'' and B'' the EJ

flares. Dark gray shading indicates topography; lighter gray shading indicates approximated

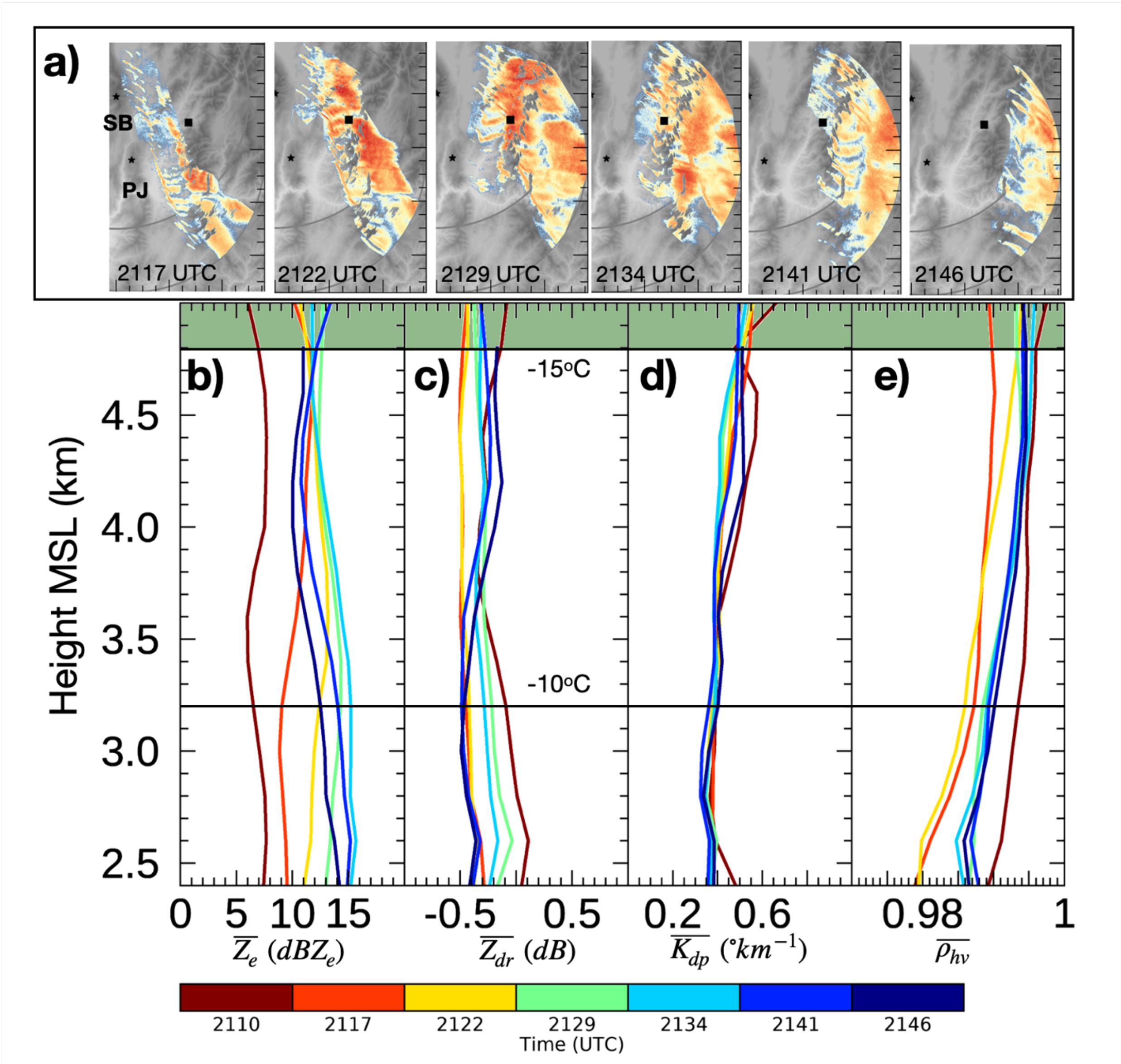

radar coverage.

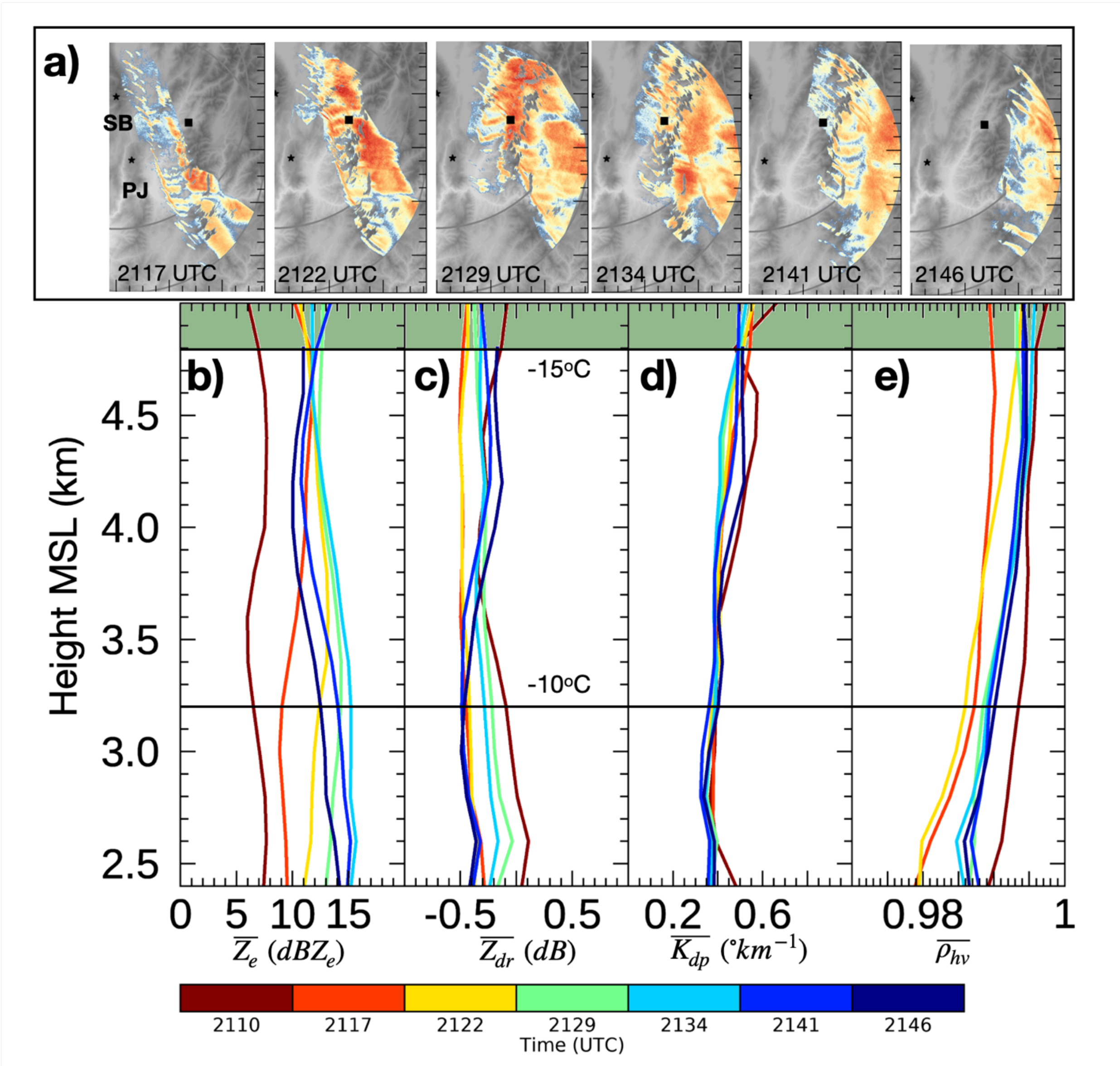

Figure 19: As Fig. 11, but showing a) PPI of Ze at 2.8 km at six radar times on 31 Jan. Each panel is 50 x 95 km. b-e) Vertical profiles of mean Z_e, Z_{dr}, K_{dp}, and ρ_{hv} over all seeding lines. Horizontal lines indicate -10, -15°C temperatures from the closest sounding at 1600 UTC sounding at Crouch. Green shading indicates the altitude range of the UWKA flight tracks.

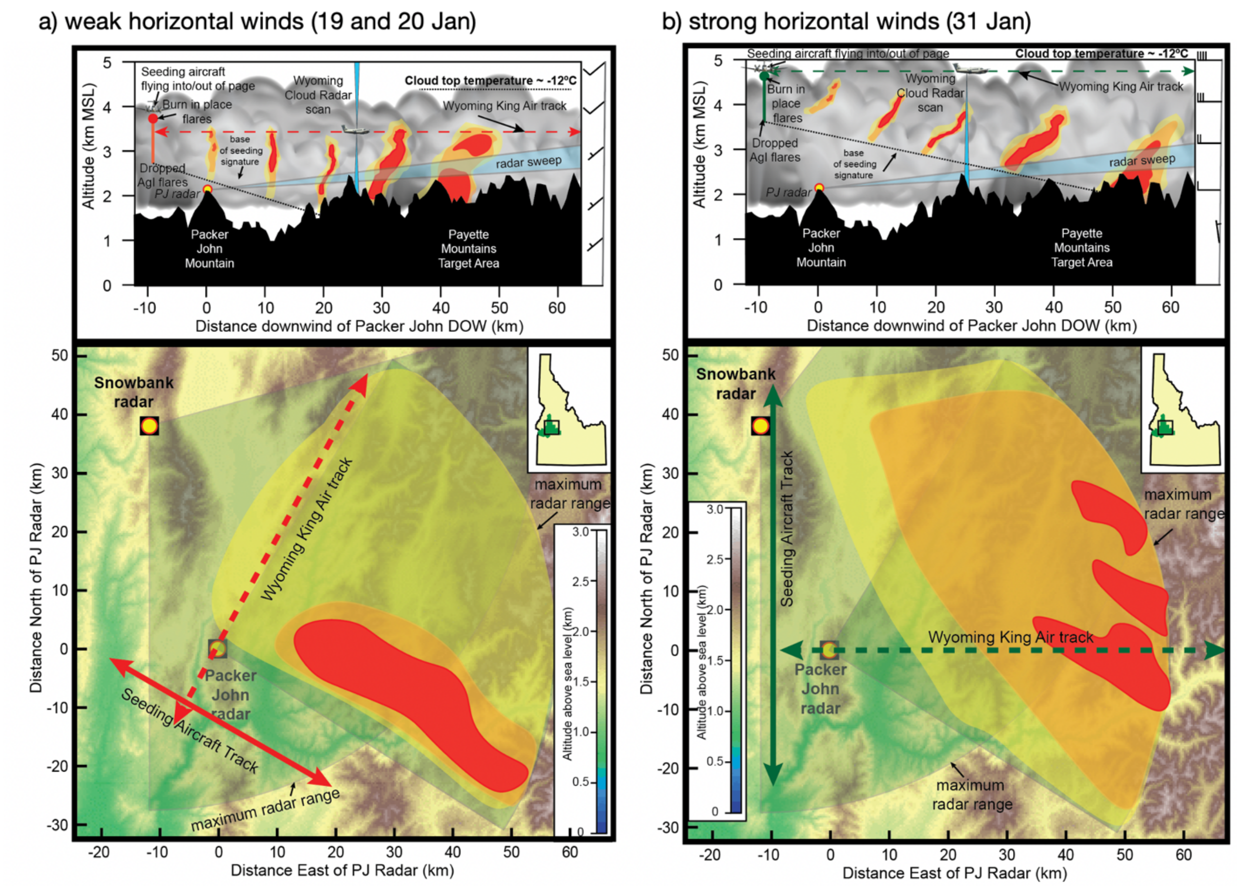

Fig. 20: A conceptual illustration of the seeding lines and snowfall with a) weak horizontal winds (19 and 20 Jan) and b) strong horizontal winds on 31 Jan (modified Fig. 1 in French et al. 2018). Top panels show temporal evolution of the seeding lines with yellow–orange–red colors indicating locations and relative magnitude of Z_e as a vertical cross section along the UWKA flight track. Bottom panels show a plain view of the distribution of total accumulated liquid equivalent snowfall with intensities increasing from yellow to orange to red colors (modified from Friedrich et al. 2020). Observations are limited to the maximum radar range; accumulations most likely occurred farther downwind and beyond the radar range. Yellow dots show locations of ground-based radars, the solid (dash) line represents a typical flight track for the seeding (Wyoming King Air) aircraft.